

## TIMING OBSERVATIONS OF PSR J1023+0038 DURING A LOW-MASS X-RAY BINARY STATE

AMRUTA JAODAND<sup>1,2,\*</sup>, ANNE M. ARCHIBALD<sup>1,2</sup>, JASON W. T. HESSELS<sup>1,2</sup>, SLAVKO BOGDANOV<sup>3</sup>, CAROLINE R. D'ANGELO<sup>4</sup>,  
ALESSANDRO PATRUNO<sup>4,1</sup>, CEES BASSA<sup>1</sup> & ADAM T. DELLER<sup>1</sup>

Draft version October 7, 2016

### ABSTRACT

Transitional millisecond pulsars (tMSPs) switch, on roughly multi-year timescales, between rotation-powered radio millisecond pulsar (RMSP) and accretion-powered low-mass X-ray binary (LMXB) states. The tMSPs have raised several questions related to the nature of accretion flow in their LMXB state and the mechanism that causes the state switch. The discovery of coherent X-ray pulsations from PSR J1023+0038 (while in the LMXB state) provides us with the first opportunity to perform timing observations and to compare the neutron star's spin variation during this state to the measured spin-down in the RMSP state. Whereas the X-ray pulsations in the LMXB state likely indicate that some material is accreting onto the neutron star's magnetic polar caps, radio continuum observations indicate the presence of an outflow. The fraction of the inflowing material being ejected is not clear, but it may be much larger than that reaching the neutron star's surface. Timing observations can measure the total torque on the neutron star. We have phase-connected nine *XMM-Newton* observations of PSR J1023+0038 over the last 2.5 years of the LMXB state to establish a precise measurement of spin evolution. We find that the average spin-down rate as an LMXB is  $26.8 \pm 0.4\%$  faster than the rate ( $-2.39 \times 10^{-15} \text{ Hz s}^{-1}$ ) determined during the RMSP state. This shows that negative angular momentum contributions (dipolar magnetic braking and outflow) exceed positive ones (accreted material), and suggests that the pulsar wind continues to operate at a largely unmodified level. We discuss implications of this tight observational constraint in the context of possible accretion models.

### 1. INTRODUCTION

Neutron stars exist with rotation rates as high as at least  $\nu_{\text{spin}} = 716 \text{ Hz}$  (Hessels et al. 2006), corresponding to a transverse velocity at the stellar equator of  $\sim 0.2 c$ . The pulsar 'recycling' mechanism is the accepted scenario for understanding how neutron stars can acquire such remarkably rapid rotation rates (Alpar et al. 1982; Radhakrishnan & Srinivasan 1982). Millisecond rotation periods can be measured directly in a number of neutron star system types: (1). radio millisecond pulsars (RMSPs), where persistent and coherent radio pulsations provide unparalleled precision on the rotational and orbital ephemeris (e.g., Ransom et al. 2014); (2). accreting millisecond X-ray pulsars (AMXPs), a type of low-mass X-ray binary (LMXB) where, occasionally, channelled accretion onto the magnetic polar caps produces coherent X-ray pulsations at the rotation rate (Patruno & Watts 2012, and references therein); and (3). LMXB burst oscillation sources, where oscillations corresponding approximately to the neutron star's rotation rate are detected during Type-I X-ray bursts (Chakrabarty et al. 2003; Watts 2012).

Direct observational evidence for the recycling scenario has recently come from the discovery of a population of transitional millisecond pulsars (tMSPs)<sup>6</sup>. The tMSPs are sources that switch between states as a rotation-powered RMSP and an accretion-powered LMXB. Three

confirmed tMSPs are known: PSR J1023+0038 (Archibald et al. 2009), XSS J12270-4859 (Bassa et al. 2014), and IGR J18245-2452 (Papitto et al. 2013a). One additional candidate tMSP, 1RXS J154439.4-112820, has also been proposed (Bogdanov & Halpern 2015). Although this source shows remarkably similar observational phenomena to the known tMSPs, it has so far only been observed in the LMXB state and its rotational period remains unknown. Thus far, all three known tMSPs are eclipsing 'redback' millisecond pulsars with non-degenerate  $\sim 0.2 M_{\odot}$  companions (Roberts 2013). This suggests that other known redback pulsars may also transition to accreting states<sup>7</sup>. Conversely, while in their LMXB state, the radio pulsar is no longer detected (even up to relatively high radio frequencies of  $\sim 5 \text{ GHz}$  and using the 305 m Arecibo telescope, Stappers et al. 2014), but a host of new, multi-wavelength observational phenomena are seen, as we describe below.

PSR J1023+0038 (hereafter J1023) is the best-studied tMSP, and detailed observations are aided by its proximity to the Earth ( $d = 1368_{-39}^{+42} \text{ pc}$ , as determined by a radio interferometric measurement of geometric parallax, Deller et al. 2012). A long-term, radio-derived timing solution has provided precise rotational and orbital parameters for the system (Archibald et al. 2013). While visible as an RMSP, J1023 shows orbital modulation of its optical and X-ray brightness (orbital period  $P_{\text{orb}} = 4.8 \text{ hr}$ ). The X-ray modulation is likely the result of the X-rays being produced in a shock near the companion's pulsar-facing side, which is partially eclipsed during the orbit

<sup>7</sup> Less clear is whether the eclipsing RMSPs known as 'black widows', which have  $\ll 0.1 M_{\odot}$  degenerate companions, will turn out to be tMSPs as well. The canonical AMXP, SAX J1808.4-3658, is black-widow-like, and previous authors presented evidence that it turns on as a rotation-powered RMSP during X-ray quiescence (Burdert et al. 2003, though no radio pulsations have yet been observed). On the other hand, many known black widows in the RMSP state have been found to be under-filling their Roche lobe in at least some cases (e.g., Breton et al. 2013), suggesting that a transition to active accretion is unlikely in those cases.

<sup>1</sup> ASTRON, the Netherlands Institute for Radio Astronomy, Postbus 2, 7990 AA, Dwingeloo, The Netherlands

<sup>2</sup> Anton Pannekoek Institute for Astronomy, University of Amsterdam, Science Park 904, 1098 XH, Amsterdam, The Netherlands

<sup>3</sup> Columbia Astrophysics Laboratory, Columbia University, 550 West 120th Street, New York, NY 10027, USA

<sup>4</sup> Leiden Observatory, Leiden University, PO Box 9513, NL-2300 RA Leiden, The Netherlands

\* To whom correspondence should be addressed; E-mail: jaodand@astron.nl

<sup>6</sup> An earlier link was also established by the discovery of the first AMXP, SAX J1808.4-3658 (Wijnands & van der Klis 1998).

(Bogdanov et al. 2011). The shock is created by the interaction of the pulsar and companion winds, and heats the companion’s face such that the optical light curve is also modulated at the orbital period (Breton et al. 2013; Thorstensen & Armstrong 2005).

J1023 transitioned to an LMXB state in 2013 June (Stappers et al. 2013; Takata et al. 2014; Patruno et al. 2014; Stappers et al. 2014), and remains in this state until now (2016 May). The state transition was signaled by the disappearance of the radio pulsar, as well as a sudden enigmatic brightening in  $\gamma$ -rays by a factor of  $\sim 5$  (Stappers et al. 2014). Though the radio pulsar is no longer detectable, a variable, flat-spectrum radio continuum source, which is suggestive of a collimated outflow, has appeared (Deller et al. 2015). Coherent X-ray pulsations have also been detected and interpreted as originating from heating of the magnetic polar caps by inflowing accretion material (Archibald et al. 2015). This means that J1023 is also an AMXP, albeit at X-ray luminosities much lower than previously observed in other AMXPs (here  $L_X \sim 10^{33}$  erg s $^{-1}$  compared to  $L_X \sim 10^{35-36}$  erg s $^{-1}$  seen in other, more distant sources while they are in outburst).

During J1023’s LMXB state, the X-ray brightness switches between three reproducible luminosity modes<sup>8</sup>: (1). high-mode ( $L_X \sim 10^{33}$  erg s $^{-1}$ ), present  $\sim 70 - 80\%$  of the time; (2). low-mode ( $L_X \sim 5 \times 10^{32}$  erg s $^{-1}$ ), present  $\sim 20\%$  of the time; and (3) occasional flares ( $L_X \sim 5 \times 10^{34}$  erg s $^{-1}$ ) present for about 2% of the time. The coherent X-ray pulsations appear only in the high mode. We note that XSS J12270–4859 also shows a highly similar behavior with three modes of X-ray brightness and coherent X-ray pulsations in high mode (Papitto et al. 2015).

The wealth of observational phenomena seen in J1023 provides many clues as to the nature of the accretion in the LMXB state, though no single, self-consistent picture has yet emerged (nonetheless, see Stappers et al. 2014; Coti Zelati et al. 2014; Archibald et al. 2015; Patruno et al. 2014; Takata et al. 2014; Tam et al. 2014; Papitto & Torres 2015; Bednarek & Banasiński 2015; Bednarek 2015, for interpretations of the observed phenomena). Importantly, the aforementioned observational phenomena seen in J1023 have also been observed in the other two known tMSPs, XSS J12270–4859 and IGR J18245–2452, as well as the tMSP candidate 1RXS J154439.4–112820. As such, though the tMSPs have suddenly presented many new puzzles, they have at least presented a consistent observational picture that can be used as the foundation for building our theoretical understanding.

A primary question is: what causes the transitions between RMSP and LMXB states? These occur rapidly (within at most weeks; Papitto et al. 2013a,b; Stappers et al. 2014), and the states themselves last for months to years (as of this writing, J1023 has been in its current LMXB state for close to 3 years). The nature of the accretion during the LMXB state is also an intriguing open question: we know that it is relatively stable on month to year timescales but that there is likely both inflow and outflow of material and the X-ray light curves switch between three luminosity modes on timescales of minutes to hours (Patruno et al. 2014; Bogdanov et al. 2015). These, and other related questions, hold the promise of coming to a much deeper understanding of pulsar recycling.

Furthermore, the tMSPs may prove to be valuable laborato-

<sup>8</sup> As in previous works (e.g., Bogdanov et al. 2015), we explicitly use the term ‘state’ to refer to the RMSP and LMXB states of the system, whereas we used the term ‘mode’ to distinguish between the three modes of X-ray brightness seen during the LMXB state.

ries for studying accretion onto magnetized compact objects in a more general sense. We aim to distinguish between plausible accretion models such as propeller mode accretion (Illarionov & Sunyaev 1975; Spruit & Taam 1993), the trapped disk scenario (Sunyaev & Shakura 1975; D’Angelo & Spruit 2011), a radiatively inefficient accretion flow model (Rees et al. 1982; D’Angelo et al. 2015), etc.

A crucial contribution toward this will come from determining how the neutron star spin changes during its LMXB state compared to its RMSP state—where the spin-down is determined to high precision using coherent timing of the radio pulsations. If the observed coherent X-ray pulsations (Archibald et al. 2015) indeed come from channelled accretion onto the magnetic poles of the neutron star, then this would in principle induce a spin-up torque (though such a torque could be modest if the accretion rate onto the neutron star is very small). Conversely, the observed radio continuum emission from a collimated outflow (Deller et al. 2015) suggests a spin-down torque due to infalling material being ejected by interactions with the rapidly rotating neutron star magnetosphere. In the RMSP state, spin-down is dominated by the pulsar wind mechanism. While some authors (e.g. Shvartsman 1971; Burderi et al. 2001) have suggested that accretion should deactivate this mechanism, others (Parfrey et al. 2015) have suggested that the spin-down could be enhanced if the accretion disk leads to the opening of previously closed magnetic field lines in the neutron star magnetosphere.

To quantitatively address these questions, we have performed an X-ray timing campaign on J1023 using *XMM-Newton*. J1023 is the only known tMSP that is currently in the LMXB state and for which we also have a precise rotational and orbital ephemeris from the previously observed RMSP state. In 2014 November/December, we acquired a pseudo-logarithmically spaced set of four *XMM-Newton* observations, which permitted us to achieve a first phase connection of the X-ray pulsations. We further extended this data set with three *XMM-Newton* observations taken a year later in 2015 November/December. Combined with earlier *XMM-Newton* observations from 2013 and 2014, we have created a simple timing model that apparently phase-connects across the entire LMXB state observed from 2013 until now.

In §2 we present these observations and a basic data analysis; §3 describes the methodology used to time the coherent X-ray pulsations and presents the results so obtained. §4 discusses the implications of these results in the context of various theoretical models. Lastly, in §5 we provide a synopsis of the main results and an outline for future work.

## 2. OBSERVATIONS & BASIC ANALYSIS

### 2.1. *XMM-Newton* Timing Observations

Though J1023 has previously been observed with *XMM-Newton* in the LMXB state (e.g., Bogdanov et al. 2015), we acquired a new set of shorter observations—presented here for the first time—with a specific cadence to allow an unambiguous phase connection of the X-ray pulsations (i.e. an accounting of all neutron star rotations over the full span of observation). A detailed explanation of the observing cadence is given in §2.4.

Firstly, J1023 was observed with *XMM-Newton* on four occasions at the end of 2014: November 21 (ObsID 0748390101), November 23 (0748390501), November 28 (0748390601), and December 17 (0748390701) as a part of the Director’s Discretionary Time (DDT) program. These observations resulted in 32, 33, 17, and 32 ks of effective exposure (EE), respectively,

and established a month-long timing baseline. The EE here refers to ‘Good Time Intervals’ (GTIs) during which the telescope was actually collecting data. There was no filtering of flares extrinsic to J1023, as it was deemed unnecessary for the analysis presented here.

A second group of closely spaced observations also became available in 2015, where J1023 was observed with *XMM-Newton* on November 11 (ObsID 0770581001, EE: 32.4 ks), November 13 (0770581101, EE: 24 ks), and December 12 (0783330301, EE: 27 ks). This established a second month-long baseline of dense observations.

For all exposures, the European Photon Imaging Camera’s (EPIC) MOS1 and 2 detectors (Turner et al. 2001) were set up in ‘Small Window’ mode to mitigate the deleterious effect of photon pileup. The EPIC pn detector (Strüder et al. 2001) was configured for the ‘Fast Timing’ mode, which offers a readout time of 30  $\mu$ s by sacrificing one imaging dimension. During all seven observations, the co-aligned *XMM-Newton* Optical Monitor (Mason et al. 2001) acquired photometric data in the *B*-band filter in the high-cadence ‘Image Fast’ mode. All the cameras were used with the thin optical blocking filter.

A summary of all existing *XMM-Newton* timing mode observations of J1023, during both its current LMXB state and previous RMSP state, can be found in Table 1. For simplicity, we have numbered these in Table 1 and will refer to these as Obs. 1 – 10 for the rest of the paper. Obs. 1, taken 2008 Nov (ObsID 0560180801), is the only *XMM-Newton* timing mode observation available during the previous RMSP state (Archibald et al. 2013). The archival data also includes Obs. 2 and 3, two longer observations acquired in 2013 Nov (ObsID 0720030101) and 2014 June (ObsID 0742610101), when J1023 was in its current LMXB state (Archibald et al. 2015; Bogdanov et al. 2015). In this work, we also include these two long observations to constrain J1023’s timing behavior as an LMXB. Thus, we have used all the nine *XMM-Newton* observations of J1023 (see Table 1) to construct a timing solution in the LMXB state.

## 2.2. Other Monitoring Observations

We are currently running a monitoring campaign with the 305 m Arecibo radio telescope in Puerto Rico to look for a switch of J1023 back to the RMSP state (or to see whether radio pulsations are intermittently detected in the LMXB state). With Arecibo, we have observed J1023 since 2014 July for 71 hr total to date, with an integration time of  $\sim 0.5 - 1$  hr per session. A detailed account of the observational setup will be provided in our upcoming paper. We are observing the source up to 5 GHz central frequency. The relatively high observing frequency is chosen to mitigate the effects of eclipses due to intra-binary material (see Archibald et al. 2009). We folded each of the observations using the *dpsr* package (van Straten & Bailes 2011) and the known radio timing ephemeris (see §2.5 for details). A visual inspection of the resulting data cubes shows no obvious signs of the radio pulsar signal (see Stappers et al. 2014), though we caution that variations in the orbit mean that the radio ephemeris is not accurate at predicting orbital phase and phase shifts of the pulsations as a function of time are expected (see §2.6). J1023 is also monitored at lower observing frequencies with the 76 m Lovell Telescope at the Jodrell Bank (400 MHz bandwidth at 1500 MHz center frequency, at roughly weekly cadence).

In parallel, since 2015 October, we have been monitoring the stability of J1023’s X-ray luminosity using *Swift*-XRT target of opportunity observations. The 26 roughly 1 ks observations

show a relatively stable flux (modulo the high/low modes and flares) at a level expected for the LMXB state. We also constructed a light curve<sup>9</sup> (binned per observation) for all the *Swift* observations since J1023 transitioned to an LMXB state in 2013. We see that the count rates have remained stable over the course of the past 2.5 years. In addition to the less frequent *XMM-Newton* observations, this further confirms that J1023 has not transitioned to an RMSP state since 2013 June, and has remained stable in its X-ray properties.

## 2.3. Preparation of XMM-Newton Data

The *XMM-Newton* data products presented here were processed using the Science Analysis Software<sup>10</sup> (SAS) version 20141104\_1833-14.0.0. The EPIC event lists were filtered using the recommended FLAG and PATTERN ranges. For our analysis we only used photons in the energy range 0.3 – 10 keV. The X-ray source and background events for each observation were obtained using the same extraction regions as in Archibald et al. (2015). The OM photometric data were extracted using the *omfchain* processing pipeline in SAS. The times of all photon event lists and time series light curves were translated to the solar system barycenter using the DE405 solar system ephemeris and the VLBI astrometric position of J1023 from Deller et al. (2012).

Figure 7 presents the X-ray and optical light curves obtained in each of the seven observations from 2014 and 2015. The light curves show great similarity to the previously observed light curves for J1023 from the longer *XMM-Newton* observations in the preceding 1.5 years of the LMXB state (Archibald et al. 2015; Bogdanov et al. 2015). In other words, the same three luminosity modes are present with approximately the same duty cycles and at roughly the same luminosities (except in Obs. 5 and 6 where no flares are detected)—suggesting that the system’s state has remained very stable. Moreover, in Fig. 7, we compare the X-ray and optical brightness. We note, e.g., that a long string of flares in the X-ray data also corresponds to observed optical flaring.

## 2.4. Motivation for Chosen Observing Strategy

The four-observation campaign conducted in 2014 was designed in order to ensure that we could construct a phase-coherent model for the neutron star’s rotation that would be valid for at least the time-span covered by these four observations themselves (roughly a month). A phase-coherent model compares the rotational phase at multiple epochs and unambiguously counts each individual rotation of the neutron star. As such, it provides much higher precision than an incoherent timing approach, i.e. one in which the observed rotational period is compared between epochs. This precision is critical for placing a meaningful constraint on whether the neutron star’s spin evolution rate has appreciably changed between the RMSP and LMXB states.

The chosen strategy employed pseudo-logarithmically spaced observations, separated by intervals of roughly 2, 5, and 19 days (see exact dates in §2.1) in order to ensure phase connection: the idea being that, once phase connection could be unambiguously achieved between the most closely spaced observations, subsequently a refined model could be obtained

<sup>9</sup> Constructed using *Swift*-XRT data products generator, an online data analysis tool offered by the UK *Swift* Science Data Centre.

<sup>10</sup> The *XMM-Newton* SAS is developed and maintained by the European Space Astronomy Centre and the Survey Science Centre at the University of Leicester.

using the larger spacings. The individual observation durations of  $\sim 32$  ks were chosen to ensure an accurate spin period determination and high signal-to-noise-ratio (S/N) pulse profile for each individual observation.

Another crucial consideration is the fact that J1023's orbital parameters vary significantly on month-long timescales (Archibald et al. 2009, 2013), meaning that the exact orbital parameters must be determined at each observing epoch in order to accurately fold the data at the 1.69 ms spin period. This can be achieved with high precision because each  $\sim 32$  ks *XMM-Newton* observation represents close to two times the 4.8-hr orbital period of J1023, thus removing covariances when modeling orbital variation via a changing  $T_{\text{asc}}$  at each epoch. Nevertheless, we still test for the possibility and significance of such covariances and show them to be unimportant (see §2.6).

The three short observations in 2015 were spaced by 2 and 26 days (see §2.1 for details). These observations approximately conform to the optimized strategy for the 2014 observation campaign described above and also allow for a phase connection to be established given prior constraints. Similarly, their average observation time of  $\sim 28$  ks, is also sufficient to robustly model the varying orbit at each epoch.

From the instrumental side, there are important limitations and uncertainties on the accuracy and precision of the EPIC-pn timing mode. First of all—due to multiple factors such as spacecraft clock issues, observation to UTC time conversion, ground station delays, spacecraft orbital ephemeris, etc.—there is a  $\pm 48 \mu\text{s}$  uncertainty ( $1 \sigma$  scatter) on the absolute time stamp associated with the beginning of each observing session (Martin-Carrillo et al. 2012). This dominates the uncertainties on our pulse phase measurements. Second, there is also a clock drift during EPIC-pn observations, conservatively determined to be  $< 10^{-8} \text{ ss}^{-1}$  by Martin-Carrillo et al. (2012). For a 30 ks observation, a clock drift of  $10^{-8}$  would smear the pulse profile by 0.3 ms, which is  $0.18 \times$  J1023's 1.69-ms pulse period. However, the simple fact that we can detect unsmearred pulsations using a constant pulse period within each observing session suggests that the clock drifts by  $\ll 10^{-8} \text{ ss}^{-1}$ . Work is ongoing to provide quantitative limits, and early results corroborate the idea that the clock drift is unimportant for the work presented here (M.Cruces et al., in prep.).

### 2.5. Prior Timing Information

The previously published radio timing of J1023 forms the input rotational and orbital model for the X-ray timing analysis presented here, as well as the spin-down model to which it will be compared (Archibald et al. 2013). This ephemeris was obtained via long-term timing observations of J1023 in the RMSP state, conducted for four years using Arecibo, the Lovell, the Green Bank Telescope (GBT), and the Westerbork Synthesis Radio Telescope (WSRT). Table 2 presents this as the fiducial ephemeris used in our analysis. We note that it differs from the ephemeris present in Table 1 of Archibald et al. (2013) because we exclude the orbital period derivative (since orbital period variations do not appear to be deterministic, and thus do not extrapolate well) and thus we have converted the ephemeris so that the epoch of spin frequency determination is the moment of disappearance.

### 2.6. X-ray Pulsation Search

The aforementioned fiducial ephemeris (see, §2.5 and Table 2) was used to assign rotational phases to the individual X-ray photons from the analysis described in §2.3. In

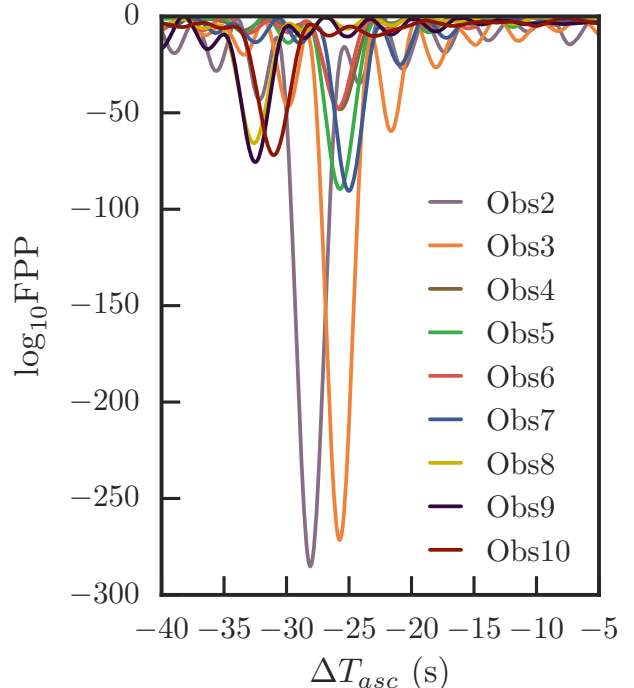


**Figure 1.** The  $H$  scores, expressed as false positive probabilities (FPPs), obtained by varying  $T_{\text{asc}}$  with respect to a reference value in each of Obs. 2 – 10. The two sets of closely spaced observations, Obs. 4 – 7 and Obs. 8 – 10, show two clusters of dips, indicating that the best-fit  $\Delta T_{\text{asc}}$  does not vary substantially during these month-long campaigns. The FPPs are naturally smaller for Obs. 2 and 3 because these are  $\sim 4\times$  longer than the short observations from the two dense campaigns.

order to search for X-ray pulsations in the presence of non-deterministic orbital period variations (see Archibald et al. 2013) we allowed for variation of the fiducial ephemeris, which resulted in the radio-derived ephemeris, also presented in Table 2. Since each of our observations spanned at least one orbital period, we were able to select the orbital parameters that maximized the significance of the detected pulse profile. Although Archibald et al. (2013) established that the orbital variations were adequately modeled by varying the time of the ascending node ( $T_{\text{asc}}$ ), we tested the effect of varying the projected semi-major axis ( $x$ ) as well. We found that this second parameter did show statistically significant stochastic variations at the tens-of-microseconds level, but the impact of fitting for it on the derived pulse phases was unimportant.

We therefore fit only for variations in  $T_{\text{asc}}$ , exploring a range of  $\pm 40$  s and selecting the  $T_{\text{asc}}$  that yielded the best  $H$  score (corresponding to false positive probabilities ranging from  $10^{-50}$  to  $10^{-300}$ ; de Jager et al. 1989). Fig. 1 shows that this allows us to unambiguously determine  $T_{\text{asc}}$ , and Fig. 2 compares these best-fit  $T_{\text{asc}}$  values to the values obtained from radio timing in Archibald et al. (2013). It also shows two different parabolic fits in radio and X-ray states to these best-fit  $T_{\text{asc}}$  values.

Using the best-fit value for  $T_{\text{asc}}$  in each observation and combining them with the radio-derived ephemeris in Table 2, we constructed nine refined local ephemerides for J1023 and successfully detected X-ray pulsations at the expected level, as shown in Fig. 3. The individual best  $T_{\text{asc}}$  values for all *XMM-Newton* observations (including the prior two observations in the LMXB state) are listed in Table 1.

**Table 1**  
Summary *XMM-Newton* Timing Mode Observations of J1023

Obs.	<i>XMM</i> Obs Id	Obs. Date	Obs. Start Time (MJD)*	Dur. (ks)	Phase Shift	$\Delta T_{\text{asc}}$ (secs)	$L_x$ High Mode ( $10^{33}$ erg/s)	$L_x$ Low Mode ( $10^{33}$ erg/s)
RMSP State Observation (presented in Archibald et al. (2010))								
1	0560180801	2008-11-26	54796.310289	34.5	-	-	0.094 (6)	
AMXP State: Long observations (those presented in Archibald et al. (2015) and Bogdanov et al. (2015))								
2	0720030101	2013-11-10	56606.765729	138	$0.0000 \pm 0.0286$	$-28.1 \pm 0.04$	$3.17 \pm 0.02$	$0.54 \pm 0.01$
3	0742610101	2014-06-10	56818.180417	131	$0.8913 \pm 0.0285$	$-25.7 \pm 0.05$	$3.06 \pm 0.02$	$0.45 \pm 0.01$
AMXP State: Short observations (those presented here for the first time)								
Short observations 2014								
4	0748390101	2014-11-21	56982.797081	35.7	$0.4307 \pm 0.0302$	$-25.7 \pm 0.24$	$3.30 \pm 0.04$	$0.43 \pm 0.02$
5	0748390501	2014-11-23	56984.791808	36.2	$0.4540 \pm 0.0285$	$-25.7 \pm 0.10$	$2.97 \pm 0.03$	$0.49 \pm 0.02$
6	0748390601	2014-11-28	56989.942650	22.0	$0.4508 \pm 0.0285$	$-25.9 \pm 0.18$	$3.08 \pm 0.05$	$0.36 \pm 0.02$
7	0748390701	2014-12-17	57008.683583	35.8	$0.4357 \pm 0.0285$	$-25.0 \pm 0.09$	$3.12 \pm 0.03$	$0.41 \pm 0.02$
Short observations 2015								
8	0770581001	2015-11-11	57337.840522	32.4	$0.2224 \pm 0.0288$	$-32.6 \pm 0.09$	$3.09 \pm 0.04$	$0.43 \pm 0.03$
9	0770581101	2015-11-13	57339.169811	24.0	$0.2806 \pm 0.0287$	$-32.5 \pm 0.09$	$3.27 \pm 0.04$	$0.34 \pm 0.03$
10	0783330301	2015-12-09	57365.070413	27.7	$0.1587 \pm 0.0286$	$-31.0 \pm 0.09$	$3.11 \pm 0.03$	$0.45 \pm 0.03$

\*Start time corresponding to the EPIC-PN in fast timing mode with the THIN1 filter. All the times of photon event lists are barycentered.

Luminosities quoted here are unabsorbed luminosities based on the known parallax distance for J1023 from Deller et al. (2012). The luminosities were obtained from spectral fits to the MOS1/2 data as shown in Bogdanov et al. (2015) and their uncertainties are estimated at a 90% confidence level.

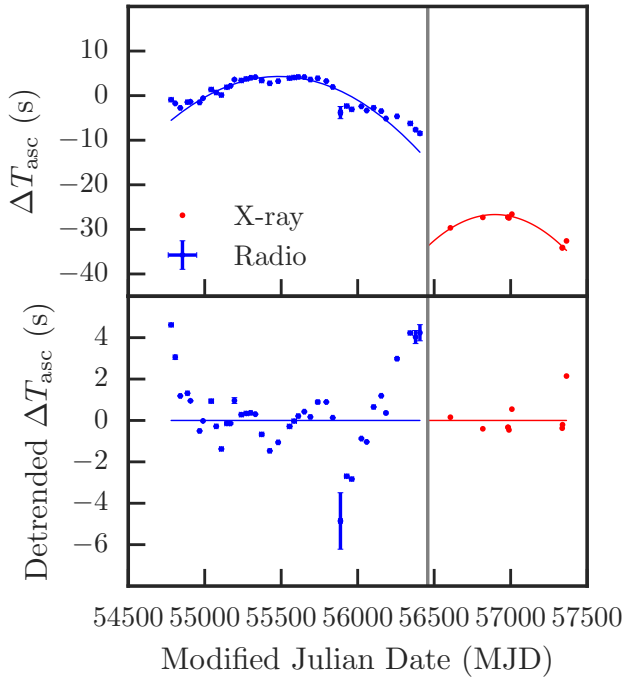


**Figure 2.** Variation in the time of the ascending node,  $\Delta T_{\text{asc}}$ , with respect to an arbitrary reference point. *Top panel:* raw  $\Delta T_{\text{asc}}$  values during both the radio (blue with horizontal lines to denote the time over which the orbit was fit; see Archibald et al. 2013) and X-ray (red) timing epochs. The gray vertical band indicates the state transition from an RMSP to an LMXB state in 2013 June. The blue and red parabolae indicate the best-fit parabolae to the radio and the X-ray measurements, respectively. We ascribe no direct physical meaning to these orbital period derivatives. *Bottom panel:*  $\Delta T_{\text{asc}}$  values after removing the best-fit parabolae to the radio and X-ray measurements. This figure is an extended version of that presented in Fig. 1 of Archibald et al. (2015), which included the first two X-ray-derived points in the LMXB state.

### 3. TIMING ANALYSIS & RESULTS

With X-ray pulsations detected in each of the Obs. 2–10, we are almost ready to use these to measure the average evolution of the neutron star’s spin rate during the LMXB state. The next step is to extract pulse phase information from every observation, as we now describe.

#### 3.1. Computing Per-observation Rotational Phase Shifts

As a first test, we can simply use the radio-derived ephemeris, with  $T_{\text{asc}}$  adjusted as described in §2.6, to fold the photons from all the nine observations. This folding procedure uses `tempo` ((Taylor & Weisberg 1989); we also used `tempo2`, (Hobbs et al. 2006; Edwards et al. 2006), for testing) to compute arrival phases for all photons, with respect to a phase reference. After this initial folding, the closely spaced observations Obs. 4–7 were remarkably well aligned, showing that there is a very little phase drift over the course of the  $\sim 1$  month spanned by these observations. This already implies that the spin evolution rate of the neutron star has not changed significantly with respect to the radio-derived ephemeris. In the following subsections, we leverage the full Obs. 2–10 data set in order to compute precisely by how much it has changed, taking into account the impact of the  $T_{\text{asc}}$  fitting procedure on the accuracy of the pulse arrival phases.

Our goal is to compute pulse arrival phases for each of the pulse profiles from Obs. 2–10. These phases are residuals relative to the radio-derived ephemeris, that is, phase shifts relative to a constant spin-down equal to that observed in the RMSP state. We do not assume any particular alignment between the LMXB-state X-ray profile and, the RMSP-state radio profile or the RMSP-state X-ray profile<sup>11</sup> presented in Archibald et al. (2010).

<sup>11</sup> We note that, in contrast to the coherent X-ray pulsations discussed here, the weak X-ray pulsations detected in the RMSP state are most likely not induced by heating of the magnetic polar caps through accretion.

**Table 2**  
Ephemerides for J1023

	Fiducial Ephemeris	Radio-derived Ephemeris (Used in this work)	X-ray Ephemeris
Pulsar name	J1023+0038	J1023+0038	J1023+0038
MJD range	56330.175–56458	56458–57500	56458–57500
Spin frequency ( $Hz$ ), $\nu$	592.421467941696(11)	592.421467941696(11)	592.421467941696(11)
Spin frequency derivative ( $s^{-2}$ ), $\dot{\nu}$	$-2.3985 \times 10^{-15}$	$-2.3985 \times 10^{-15}$	$-3.0413 \times 10^{-15}$
Spin period ( $ms$ ), $P$	1.68798744494252 (13)	1.68798744494252 (13)	1.68798744494252 (13)
Spin period derivative ( $s/s$ ), $\dot{P}$	$6.834 \times 10^{-21}$	$6.834 \times 10^{-21}$	$8.665 \times 10^{-21}$
Orbital period ( $d$ ), $P_{\text{orb}}$	0.1980963155	0.1980963155	0.1980963155
Time of ascending node ( $MJD$ ), $T_{\text{asc}}$	54905.97140075	*	54905.97140075
Projected semi-major axis ( $lt - s$ ), $x$	0.343356	0.343356	0.343356
Right ascension, $\alpha$	10:23:47:687198	10:23:47:687198	10:23:47:687198
Declination, $\delta$	+00:38:40.84551	+00:38:40.84551	+00:38:40.84551
Epoch of frequency determination ( $MJD$ )	56458	56458	56458
Epoch of position determination ( $MJD$ )	54995	54995	54995
Dispersion measure, $DM$ ( $\text{cm}^{-3}\text{pc}$ )	14.325299	14.325299	14.325299
Solar System ephemeris model	DE 200	DE 200	DE 200
Orbital eccentricity, $e$	0	0	0

Ephemerides for PSR J1023 + 0038. The radio-derived ephemeris is used in §3 to search for pulsations. It is based on the long-term radio timing ephemeris (referred here as the fiducial ephemeris) presented in Archibald et al. (see 2013, Table 1), but does not include an orbital period derivative (since orbital period variations do not appear to be deterministic, and thus do not extrapolate well). This ephemeris has also been used in Stappers et al. (2014) and Archibald et al. (2015). Derived as a parameter-restricted fit, it enables an accurate prediction of the pulse phase in the neutron star’s inertial frame. In our analysis, we employ this property and construct a radio-derived ephemeris by varying the  $T_{\text{asc}}$  for each one of our observations in order to account for orbital variations (see §2.6). Hence, we have marked this  $T_{\text{asc}}$  with an asterisk in the radio-derived ephemeris. Apart from the known spin period derivative from the radio state, here we also present X-ray ephemeris, which includes the spin period derivative in the LMXB state (see, §3.2 for details). We find that using only this X-ray ephemeris containing the orbital period derivative,  $\dot{P}_{\text{orb}}$  reported in §3.3, we can fully account for non-deterministic orbital variations in the LMXB state without fitting for  $T_{\text{asc}}$ . In this case, the values for  $T_{\text{asc}}$  and  $\dot{P}_{\text{orb}}$  should be taken as the ones reported in §3.3. Alternatively, we can also exclude the  $\dot{P}_{\text{orb}}$  in X-ray ephemeris and vary the  $T_{\text{asc}}$  (similar to the radio-derived ephemeris) to model the orbit in the LMXB state.

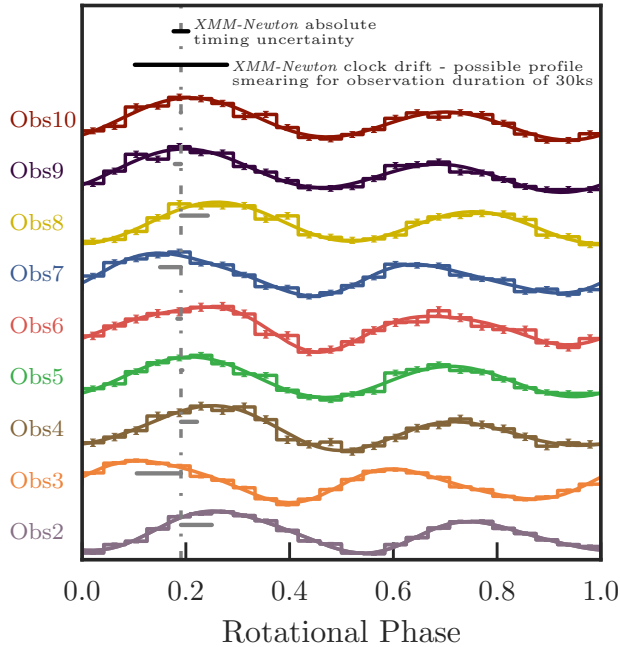


**Figure 3.** Background-subtracted, normalized pulse profiles for each of the nine *XMM-Newton* observations (from bottom to top: Obs. 2–10, see Table 1) folded using our best-fit spin-down. An arbitrary vertical offset has been added to each profile so that they do not overlap. The color code is the same as in Fig. 1. The photons were folded using the X-ray ephemeris (see Table 2) containing the spin-frequency derivative in the LMXB state, computed in §3.2,  $\dot{\nu}_{\text{LMXB}} = (-3.0413 \pm 0.0090) \times 10^{-15} \text{ Hz s}^{-1}$ . We exclude the orbital period derivative in this ephemeris and instead use the  $T_{\text{asc}}$  computed per observation as described in §2.6 to model the orbit in the LMXB state. Histograms are plotted for convenience; the smooth curves are obtained directly from photon phases (for more details, see Archibald et al. 2015) and are used in determining pulse arrival phases. After, the profiles are obtained in such a manner we re-compute their phase shifts w.r.t. Obs. 2 (chosen as a template based on its high signal-to-noise-ratio). The horizontal solid gray line shows the offsets of these phase shifts w.r.t. the average phase shift. Note that each profile’s phase is subject to an  $\sim 48\mu\text{s}$  ( $\sim 0.028 \times \text{spin period}$ ) timing uncertainty (see §2.4). This absolute timing uncertainty and the clock drift uncertainty are presented here with horizontal solid gray lines at the top of the plot.

We compute the per observation phase shifts by cross-correlation with a high-signal-to-noise template. From, the nine observations presented in Table 1, the long (138 ks) 2013 November *XMM-Newton* observation (Obs. 2) is used as a template given that it has the highest signal-to-noise-ratio. We compute the Fourier coefficients of this profile and truncate them to the four significant harmonics suggested by the *H-test*. We then use cross-correlation to optimally align this template with the similarly computed Fourier-domain profiles for each of our nine observations. The result is a phase offset for each observation.

The uncertainties in these phase shifts come from three main sources: photon scarcity, covariance with the  $T_{\text{asc}}$  fitting, and (the dominant effect) the absolute timing uncertainty of *XMM-Newton* (see §2.4). We address the first two with a bootstrap procedure (Wackernagel 2003; Cuevas & Romo 1993): we repeatedly generate simulated data sets by drawing photons from the observed photons with replacement. Then for each simulated data set we repeat the procedure of fitting for  $T_{\text{asc}}$  and then extract a pulse phase. This introduces a scatter in pulse phase of roughly  $\sim 0.0043$  turns. We then add this in quadrature to the known  $48\mu\text{s}$  absolute timing uncertainty (equivalent to 0.028 cycles) of *XMM-Newton* (Martin-Carrillo et al. 2012) to obtain the total uncertainty on each pulse phase

measurement. The results are shown in Fig. 5 and tabulated in Table 1.

### 3.2. Phase Connection and Timing

We now derive a precise measurement of the neutron star’s spin-down rate during Obs. 2–10. A change in spin-down rate compared to that predicted for the same epoch by the radio-derived ephemeris would produce a parabolic trend with time in the measured pulse phases. Therefore, in principle, we need to simply carry out a least-squares fit to the pulse phases. However, since they are phase measurements, the values shown in the insets of Fig. 5 and Table 1 are all recorded modulo one turn of the neutron star. There may therefore be an ambiguity coming from the fact that we do not know *a priori* how many times the neutron star turned between observations. The spacing of Obs. 4–7 was designed to avoid this ambiguity, but the long gaps between Obs. 2 and 3 (due to the *XMM-Newton* Sun constraint) and the non-optimal cadence of Obs. 8–10 allow for the possibility of phase wraps when trying to phase connect the full data set. Therefore, for each candidate spin-down rate, we shift the phases appropriately, wrapping them as necessary modulo the spin period, and compute the sum of squares of the normalized errors ( $\chi^2$ ).

We followed this procedure first for the dense observation sets from 2014 (Obs. 4–7) and 2015 (Obs. 8–10) individually, obtaining spin frequency measurements from each set. We then summed the two  $\chi^2$  error functions for these observation sets. The minimum of this summed function yields a change in frequency derivative corresponding to a phase connection valid only within the month-long observation sets individually, but not necessarily between them. We call this the *Short Baseline* approach. Once we could semi-coherently phase connect the two clusters of observations, we attempted phase connection between all seven observations in these two sets to arrive at  $\chi^2$  errors and corresponding minima. This resulted in a phase connection of the two observation sets separated by a year (Obs. 4–10 phase-connected), referred to here as the *Year-long Baseline* approach. Finally, in the *Full Baseline Approach*, we included all the nine *XMM-Newton* observations (Obs. 2–10) to get a corresponding  $\chi^2$  error function and establish a fully coherent phase connection valid over the past 2.5 yrs.

The  $\chi^2$  error functions for the above three approaches are shown in Fig. 4. Although there are many local minima, the absolute minima for the *Short Baseline*, *Year-long Baseline* and *Full Baseline* approaches all match at a value close to  $\dot{\nu}_{\text{LMXB}}/\dot{\nu}_{\text{RMSP}} = 1.27$  (i.e. there is no combination of additional phase wraps that improve upon this solution). Although searching over an even wider range of spin-down rates could in principle produce an even better fit to the measured phases, greater frequency derivative changes than considered would be apparent in our folding of single observations and are thus ruled out (even given the claimed relative clock drift of *XMM-Newton*; Martin-Carrillo et al. 2012). We are therefore able to unambiguously phase-connect all the nine *XMM-Newton* observations obtained during the last 2.5 years of J1023’s LMXB state.

Having established the number of phase wraps relative to the radio ephemeris, we are able to fit a model to the pulsar’s spin-down. We choose a model in which the spin frequency derivative is constant during the LMXB state but is different from that during the RMSP state. We also assume that the spin frequency is continuous (that is, it does not jump at the moment of RMSP to LMXB state transition in 2013 June), but we do not assume any phase relationship between the LMXB

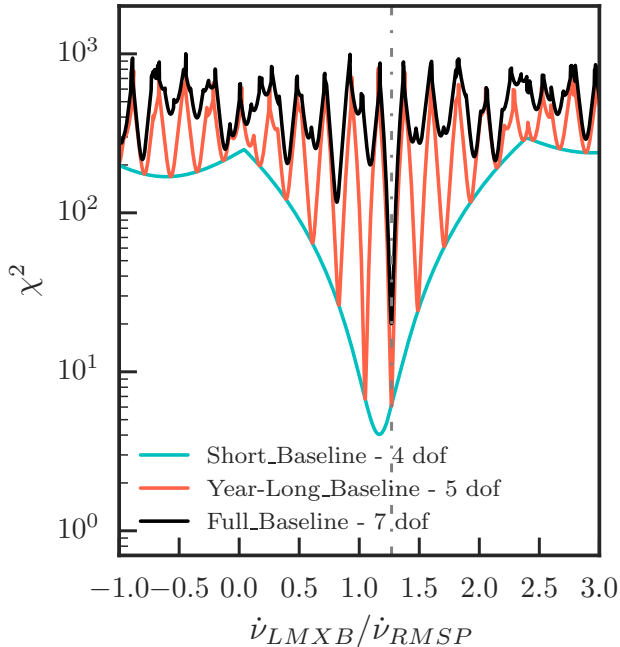


**Figure 4.**  $\chi^2$  values for a range of LMXB-state spin frequency derivatives,  $\dot{\nu}_{\text{LMXB}}$ . Here, the gray dotted-dashed line marks the new value of the observed spin frequency derivative obtained from the coincidence of the dips in  $\chi^2$  error functions for various phase connection baselines. Uncertainty on this value differs for each phase connection baseline and is obtained from the change in frequency derivative, which increase the minimum  $\chi^2$  value by one. Finally, we also list degrees of freedom (dof) associated with each phase connection baseline.

and RMSP states. The change in spin frequency derivative we obtain in this constant spin-down model is  $\dot{\nu}_{\text{LMXB}}/\dot{\nu}_{\text{RMSP}} = 1.268 \pm 0.004$ , as shown in Fig. 5. J1023’s spin-down rate since transition from RMSP to LMXB is therefore  $\dot{\nu}_{\text{LMXB}} = (-3.0413 \pm 0.0090) \times 10^{-15} \text{ Hz s}^{-1}$ .

The reduced  $\chi^2$  of this fit is 2.87 with seven degrees of freedom, which corresponds to a false positive probability of 0.005. Finally, we estimate our uncertainties as the range of  $\dot{\nu}_{\text{LMXB}}/\dot{\nu}_{\text{RMSP}}$  values that increase the (non-reduced)  $\chi^2$  by no more than one. Using this technique for the three phase connection approaches: *Short Baseline*, *Year-long Baseline* and *Full Baseline*, we get uncertainties of 7.17%, 0.49%, and 0.38%, respectively. Including the two long observations, Obs. 2 and 3, does not introduce a major change in the uncertainty on the frequency derivative estimate because these observations are closest to the time of state transition. Also, though we deem it unlikely, if one assumes that only the *Short Baseline* approach is robustly phase-connected then J1023 is still measured to be spinning down faster in the LMXB state at the 3.5- $\sigma$  level.

### 3.3. Alternative Orbital Modeling

Toward the late stages of this work we realised that we could essentially obtain an orbital period derivative in the the LMXB state by fitting a parabola to the time of ascending nodes for Obs. 2 – 10 (reported in Table 1). Although we attribute no physical significance to this value, this orbital period derivative ( $-1.65(0.19) \times 10^{-10} \text{ day/day}$ , as shown by the red parabolic fit to X-ray measurements in Fig. 2) taken together with the X-ray ephemeris (Table 2) containing time of ascending node and orbital period ( $T_{\text{asc}} = 54905.96943473 \text{ MJD}$  and  $P_{\text{orb}} = 0.198096646761 \text{ day}$ , respectively) from the same parabolic fit, can be used to fold the observations in the LMXB state.

The profiles, which we obtain from such a folding operation, are almost identical to the ones reported in Fig. 3. We then compute phase shifts for these profiles w.r.t Obs. 2 (used here as a template given it has the highest S/N). These post-fit phase residuals are then plotted with red color in the third panel of Fig. 5. Here, we see that the post-fit phase shift residuals obtained from modeling the non-deterministic orbital variations with X-ray ephemeris containing either (a) variation of  $T_{\text{asc}}$  or (b) the orbital period derivative, coincide. This coincidence independently corroborates our technique of varying the  $T_{\text{asc}}$  (detailed in §2.6 and the appendix A) to model the non-deterministic orbits for pulsars in binary systems such as rebacks and black widows.

Moreover, we are now using this orbital period derivative estimate to systematically fold the gamma-ray photons from the *Fermi*-Large Area Telescope, and search for gamma-ray pulsations.

### 3.4. Robustness and Potential Pitfalls

Fig. 3 shows that folding Obs. 2 – 10 with the X-ray ephemeris (listed in Table 2) without the  $\dot{P}_{\text{orb}}$  and varying the  $T_{\text{asc}}$  for each observation (as done in the case of the radio-derived ephemeris) yields well aligned pulse profiles. The X-ray ephemeris now contains the spin frequency derivative with the  $\dot{\nu}_{\text{LMXB}}$  value determined in the preceding section. We then see that as such the greatest outlier from such a folding operation is Obs. 3, which is 2.6 $\sigma$  off from the prediction of the best-fit constant spin-down model in the LMXB state (Fig. 5; middle panel). Although the total reduced chi-squared for the fit is 2.87 (with 7 degrees of freedom, corresponding to a false positive probability of 0.005), which indicates a reasonable fit, the analysis of Martin-Carrillo et al. (2012) shows a number of outlier points (see their Fig. 8), so the deviation seen in Obs. 3 may also be the result of *XMM-Newton* clock limitations.

We also point out that the three frequencies—the spin frequency at disappearance, the spin frequency obtained from observations 4–7 and that obtained from observation 8–10—lie quite exactly on a line, though the last two were computed assuming only short term phase connection within a group of observations. This supports the idea that the system is spinning down at a constant rate not very different from that seen in the radio state.

The technique of fitting for  $T_{\text{asc}}$  is new; for details, see the Appendix. Although these variations are small, it is necessary to account for them to recover the pulsations. Our bootstrapping process for error estimation accounts for the (small) impact of this fitting on the derived pulse phases.

There are at least two potential pitfalls for the analysis presented here. Firstly, *XMM-Newton* is known to occasionally experience one-second clock jumps. If one occurred near the beginning of one of our observations, without correction in post-processing, then the phase computed for that observation would be dramatically incorrect. Such jumps can be detected by adjusting post-processing parameters; we find none in Obs. 2 – 10, and the chance of a spurious phase alignment caused by such a jump is very low.

Second, we assume that the pulse phase flawlessly tracks the orientation of the neutron star. This is a standard assumption in the timing of radio pulsars, but some AMXPs show pulse profile changes, which indicate that the accretion-induced hotspots are changing size and/or location (Patruno et al. 2009; Patruno 2010; Patruno & Watts 2012). If the hotspots we observe in J1023 are wandering, then the apparent spin-down does not track the neutron star surface. Such hotspot wandering is

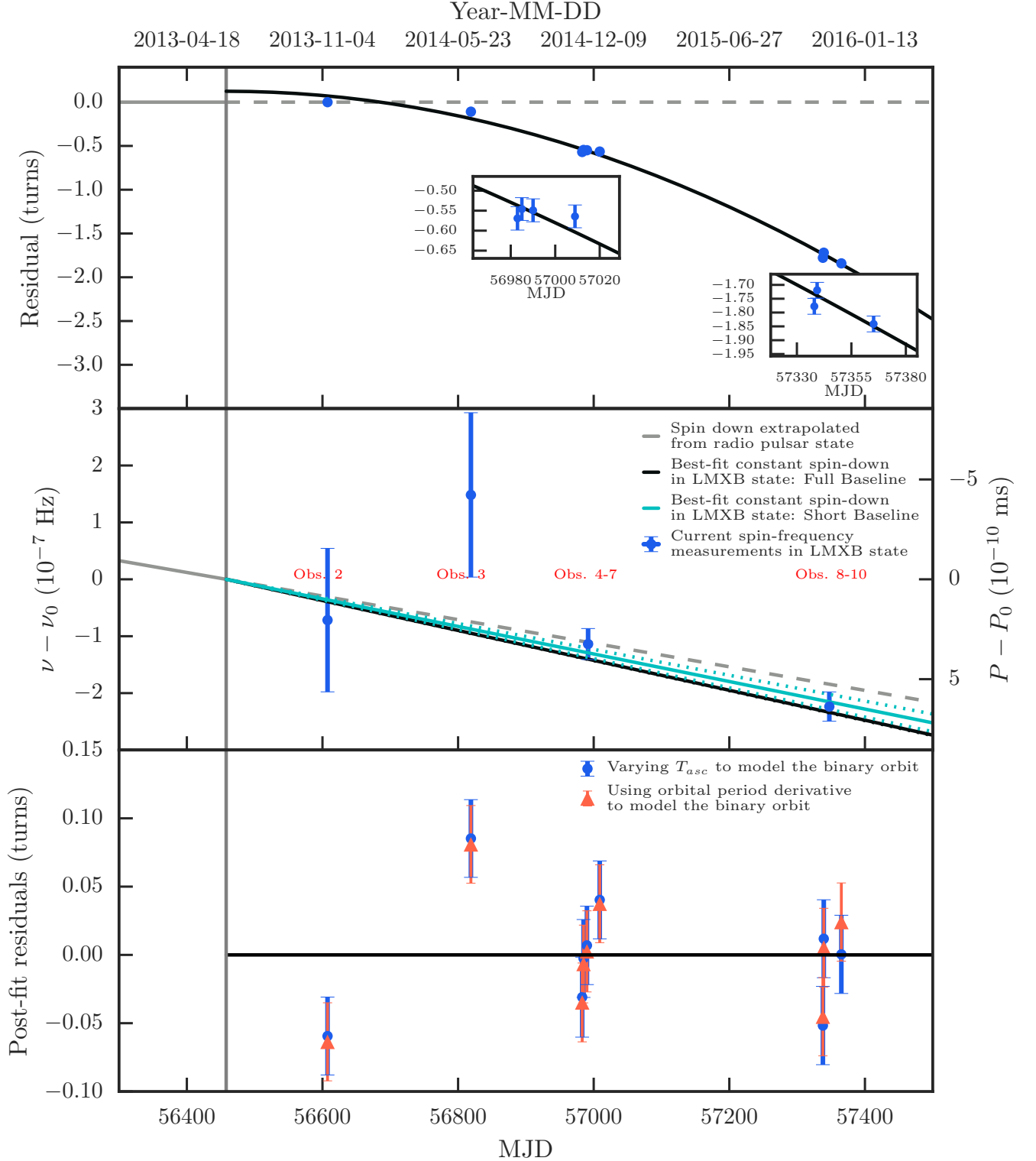


**Figure 5.** Our model for the spin evolution of J1023 and the measurements constraining it. The vertical, solid gray line in each subplot indicates the epoch of RMSP to LMXB state transition (2013 June). Other solid gray lines indicate values derived from the radio ephemeris, dashed where these are extrapolated beyond the ‘MJD range’ quoted in Table 2. The black curves indicate a post-state-transition, constant spin-down model derived from phase connecting all of observations Obs. 2 – 10 (*Full Baseline* solution as shown in Fig. 4); extended dotted black lines show  $1\sigma$  error bars. *Top panel:* phase-shift measurements from Obs. 2 – 10 (blue points) with respect to the radio-derived ephemeris. The best-fit constant spindown model is shown by the solid black line. The inset shows which observation from Table 1 each point corresponds to. When comparing to the quoted phases in Table 1, note that there have been single phase wraps removed between both Obs. 2/3 and between Obs. 3/4-7. Additionally, there have been two phase wraps removed between Obs. 4-7/8-10. *Middle panel:* spin frequency evolution. The solid line shows the derivative of the best-fit model, while data points are short-term frequency measurements. Those for Obs. 2 and 3 are computed from single observations, assuming the *XMM-Newton* clock drift is negligible, while those from Obs. 4 – 7 and 8 – 10 are obtained by phase connecting only the observations within each set. These short-term model-independent frequency measurements agree with the constant spin-down model we fit to the phases. The black and cyan color show constant spin-down models derived from *Full Baseline* and *Short Baseline* approaches, respectively. *Bottom panel:* the blue colour shows the post-fit phase shift measurements obtained from the profiles presented in Fig. 3. The post-fit residuals on fitting with an alternative method using orbital period derivative (see, Section 3.3 for the technique) are shown in red colour.

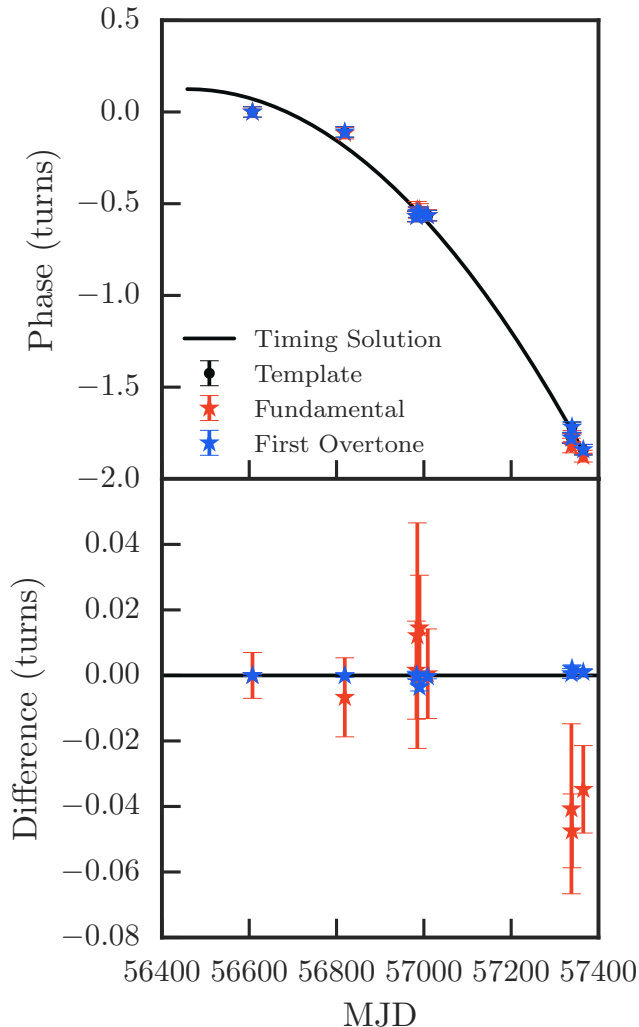


**Figure 6.** Comparison between timing with individual harmonics versus a full template pulse profile. Top panel: the pulse phases obtained by using a full template and the timing solution obtained using them are shown in black. Pulse phases obtained using the fundamental and first overtone are shown in red and blue respectively. Error bars are almost the same since they are dominated by the absolute *XMM-Newton* timing uncertainty. Bottom panel: phase differences between the template-derived phases and those obtained from the fundamental and first overtone.

usually accompanied by pulse profile variations and/or luminosity variations. We have observed that the X-ray luminosity of J1023 is remarkably constant in the low and high modes (particularly during the high mode, which is the only one that shows pulsations), and Fig. 3 shows that the pulse profiles do not vary substantially. We also verified the stability of the pulse profiles by using the standard technique of timing harmonics separately (see, [Patruno et al. 2009](#), where this technique has been used for a sample of six AMXPs). Our analysis using the fundamental and the first overtone is shown in 6. Here, we see that the pulse phases obtained from using different harmonics are consistent with each other and with template-based phases, thus rendering the timing of separate harmonics not necessary. This further highlights the stability of the pulse profiles. Moreover, it is hard to imagine that such a simple, enhanced constant spin-down model could provide such an excellent fit if the hotspot is appreciably wandering.

A lingering concern was the incorporation of Obs. 2 and 3 into our phase-coherent timing analysis. Phases determined

from these observations are broadly consistent with our best-fit model, although Obs. 3 is somewhat of an outlier, as discussed above. That said, their inclusion makes only a small difference to the best-fit spin-down and its uncertainty, since they are closest to the radio-X-ray state transition and all phase uncertainties are dominated by the *XMM-Newton* absolute clock uncertainty.

#### 4. DISCUSSION

Our phase-coherent *XMM-Newton* timing observations of J1023 during its current LMXB state indicate that the average spin-down rate is 26.8% faster than the spin-down rate during the rotation-powered RMSP state—i.e.  $\dot{\nu}_{\text{LMXB}}/\dot{\nu}_{\text{RMSP}} = 1.268 \pm 0.004$  and  $\dot{\nu}_{\text{LMXB}} = (-3.0413 \pm 0.0090) \times 10^{-15} \text{ Hz s}^{-1}$  (see Fig. 5). From this we conclude that the previous spin-down mechanism is still dominant and additional torques on the neutron star during this accreting state are modest in comparison. This somewhat surprising result has implications for both the radio pulsar mechanism and magnetospheric accretion physics. The X-ray pulsations seen in the ‘high’ mode of the accreting phase are interpreted as accretion hotspots at the magnetic polar caps ([Archibald et al. 2015](#); [Bogdanov et al. 2015](#)), but the enhanced constant spin-down rate suggests that the pulsar wind remains active and essentially unchanged even after the accretion disk forms and matter accretes onto the neutron star’s surface. This is in direct contrast with earlier predictions (e.g. [Shvartsman 1971](#); [Burderi et al. 2001](#)) that the transition to active accretion would suppress the pulsar wind. However, several authors have proposed that J1023’s pulsar has remained active but is enshrouded by intra-binary material ([Coti Zelati et al. 2014](#); [Stappers et al. 2013, 2014](#)) in the LMXB state.

##### 4.1. Stability of the System

It is again worth emphasizing how stable and predictable the behavior of J1023 has been over the course of nearly three years. In all the nine *XMM-Newton* observations in the LMXB state, those presented in [Bogdanov et al. \(2015\)](#) and those presented here, we see basically the same pulse profile morphology and pulsed-fraction. Likewise, the luminosity modes (‘low’, ‘high’) are present in all observations and flares are detected in all but two short observations (Obs. 5 and 6), at comparable luminosities. In other words, this is not a chaotic LMXB outburst, but rather a well-defined, quasi-stable (the X-ray pulsations switch on-off with the high mode) accretion regime. At the same time, though orbital variability is observed, the change in  $T_{\text{asc}}$  during the LMXB state is no more dramatic than what is seen in the non-accreting RMSP state.

##### 4.2. Comparison with the Timing of other AMXPs

Compared with other AMXP systems (see [Patruno & Watts 2012](#), for a review), where pulsations are seen in outburst at much higher X-ray luminosities<sup>12</sup> of  $10^{35-37} \text{ erg s}^{-1}$ , J1023 has the great advantage of possessing a known, high precision rotational and orbital ephemeris derived from radio timing in the RMSP state (as well as a parallax-derived distance).

Spin variation measurements of other actively accreting AMXPs is difficult because their typical outburst duration is short ( $\lesssim 1$  month). This makes any timing solution over that limited time-span insensitive to spin variations of magnitudes

<sup>12</sup> It is possible that other known AMXPs have entered an LMXB state similar to that of J1023 but their much larger distance (typically 3 – 8 kpc) has led us to miss this behavior.

comparable to what we have observed in J1023. The long-term (i.e. months to years) spin variation over periods of X-ray quiescence has been securely measured in only three systems so far (Patruno & Watts 2012). For example, SAX J1808.4–3658 is the best-timed AMXP and it has a spin-down on the order of  $10^{-15} \text{ Hz s}^{-1}$ , measured by comparing the spin frequency in six different outbursts observed over a baseline of 13 years (e.g., Patruno et al. 2012; Hartman et al. 2008; di Salvo et al. 2008). Only upper limits have been placed on the spin-up/down during an outburst. The other two AMXPs with a measured long-term spin variation also show a spin-down in quiescence that is close in magnitude to that observed in J1023 (however, they both show a moderately strong spin-up in outburst at luminosities of  $\sim 10^{36} \text{ erg s}^{-1}$ ; Patruno 2010; Papitto et al. 2011; Hartman et al. 2011; Riggio et al. 2011).

Whether the long-term spin-down observed in other AMXPs has the same physical origin as in J1023 is difficult to say at the moment, since none of these sources have been detected pulsating in radio so far and thus it is impossible to compare the observed (quiescent) long-term spin-down with a radio-derived ephemeris. The lack of observed radio and/or X-ray pulsations during quiescence in AMXPs may simply be due to their larger distances (typically 3 – 8 kpc, compared to the 1.3 kpc of J1023).

#### 4.3. The Nature of J1023’s LMXB state

J1023 spins down 26.8% faster in the LMXB state than in the RMSP state. This is measured with high precision (0.4% uncertainty) because we can phase connect all the available *XMM-Newton* observations. The corresponding spin-down rate  $\dot{\nu}_{\text{LMXB}} = (-3.0413 \pm 0.0090) \times 10^{-15} \text{ Hz s}^{-1}$ . The lack of drastic (factor of a few or more) change in spin-down between states strongly suggests that the main radio pulsar spin-down mechanism (i.e. the pulsar wind) remains active in the accreting LMXB state, and that interaction between the accretion flow and magnetic field introduces a net additional spin-down of  $\dot{\nu} \simeq -6.4 \times 10^{-16} \text{ Hz s}^{-1}$ . This observation introduces both new questions and unprecedented constraints on accretion-regulated spin change.

First of all, it is surprising that the change in magnetic field configuration needed to support accretion onto the neutron star’s surface is not accompanied by a more dramatic change in spin-down rate. Radio pulsar spin-down is chiefly determined by an outflow of relativistic particles along open magnetic field lines (Goldreich & Julian 1969). Simulations of pulsar winds show that the rotating magnetic field assumes a largely open, ‘split monopole’ configuration, with the wind strongest along the plane of rotation (e.g. Spitkovsky 2006). Simulations and analytical arguments suggest that the strength of the pulsar wind (and hence the spin-down rate) is directly proportional to the number of opened field lines, so that it scales with the area of open field lines (Spitkovsky 2006; Parfrey et al. 2015).

In the absence of an accretion disk, the magnetic field is forced open by relativistic constraints, and all the magnetic field lines that intersect the light cylinder ( $r_{\text{lc}} \equiv c/\Omega_* = 8 \times 10^6 \text{ cm}$  for J1023) will be opened and support an outflowing wind. However, the presence of an accretion disk will radically increase the number of open field lines, changing the spin-down rate and wind strength. This is because the inner edge of the accretion disk will interact with the magnetic field, and the large difference in angular velocity between the star and the disk material will tend to cause field lines to stretch and become open (Aly & Kuijpers 1990; Lovelace et al. 1995;

Uzdensky et al. 2002; Parfrey et al. 2015). A small portion of these field lines may then periodically reconnect to the disk, so that the reconnection and field line opening can lead to outflows of magnetic field and matter (e.g. Hayashi et al. 1996; Goodson et al. 1997; Miller & Stone 1997; Romanova et al. 2004; Zanni & Ferreira 2013; Lü et al. 2014; see also the review from Uzdensky 2004). As a result of the disk-field coupling, virtually all field lines that would intersect the disk will be opened and remain open, substantially increasing the spin-down rate. If the X-ray pulsations in J1023 indeed originate from accretion onto the neutron star, the accretion disk must at some times (i.e. during the ‘high’ luminosity mode) extend at least to the co-rotation radius ( $r_{\text{c}} \equiv (GM_*/\Omega_*^2)^{1/3} = 2.4 \times 10^6 \text{ cm}$ ) where the star’s spin rate equals the Keplerian disk velocity. This is roughly a third of the light cylinder radius, so that the area of the open field line region (and hence the spin-down power of the wind) should increase by up to 10 times, which is not observed.

How can this discrepancy be resolved? One speculative possibility is that the high/low modes are not the result of accretion and in fact represent an exotic example of ‘mode switching’—a poorly-understood process observed in some isolated pulsars. We discuss this further in §4.5. A second possibility is that the pulsar wind spin-down efficiency decreases during accretion episodes due to a decrease in the plasma supply to the pulsar wind. This has been suggested by Li et al. (2012) to explain variations in the spin-down rate of isolated pulsars. In this case, the extra spin-down from the increased open field line region would be offset by a reduction in spin-down from outflowing plasma. However, given that there is only a 26.8% change in spin-down rate whereas the field line opening would increase spin down by up to 10 times, it seems somewhat contrived that these two effects nearly perfectly balance each other.

We would also like to suggest that maybe a residual disk remains present even in the RMSP state so that the field configuration does not substantially change between the LMXB and RMSP state. This could happen if the interaction between the magnetic field and accretion disk allows a ‘trapped disk’ to form (Sunyaev & Shakura 1977; D’Angelo & Spruit 2010, 2011, 2012, and also below). In this model, the angular momentum added by the magnetic field at the inner edge of the disk matches the rate at which turbulence transports angular momentum outward, so that the net accretion rate through the disk is zero (this is the ‘dead disk’ density solution, which was first derived by Sunyaev & Shakura 1977). The disk could persist even when the radio pulsar is active, since the majority of the disk would be disconnected from the magnetic field and shielded from the pulsar wind by the magnetic field lines that connected to the inner edge of the disk. This solution also has observational predictions for the limits on spin change, which we discuss in §4.4.

A final consideration is the nature of the outflow from J1023. As shown in (Deller et al. 2015), radio observations of J1023 in the LMXB state reveal a variable flat-spectrum emission strongly suggestive of a jet and, considerably brighter than predicted from observations of other neutron star LMXBs accreting at higher accretion rates. Taken at face value, this implies that the accretion flow in J1023 is generating a more powerful jet than expected. While a propeller mechanism could explain the radio observations, as shown above, it should lead to a strong spin evolution, which our observations rule out. Thus, the interaction of the accretion flow with the radio pulsar in the J1023 system must both lead to a radio-bright outflow while simultaneously not greatly affecting the overall

spin-down rate.

#### 4.4. Limits on Accretion-induced Spin Modulation

The most natural interpretation for the observed additional spin-down is that it is a result of interaction of the magnetosphere with the accretion flow and the disk. Such a strong limit on accretion torques has never before been set in a millisecond pulsar, particularly not at such low luminosities. In this interpretation, the net accretion-related spindown  $\dot{\nu} = -6.4 \times 10^{-16} \text{ Hz s}^{-1}$ . Using the X-ray luminosity as a proxy for the accretion rate onto the star, the well-constrained magnetic field and rotation rate allow us to estimate the expected spin change from magnetospheric accretion.

The observed luminosity is dominated by channeled accretion onto the surface (at a rate  $\dot{M}_{\text{obs}}$ ), which spins the star up. This means that the spin-down rate is somewhat higher than is observed. To correct for this and convert the observed luminosity into an accretion rate requires some assumptions for the bolometric correction factor. [Bogdanov et al. \(2015\)](#) measured average luminosities (0.3 – 10 keV) of  $[0.54, 3, 10] \times 10^{33} \text{ erg s}^{-1}$  for the low, high and flaring states, and estimated that the source spends a  $[0.22, 0.77, 0.01]$  fraction of its time in each state, giving an average luminosity of  $L_x = 2.9 \times 10^{33} \text{ erg s}^{-1}$ . *NuSTAR* observation of J1023 showed an unbroken power law in X-ray emission extending to at least 79 keV ([Tendulkar et al. 2014](#)), which implies that the bolometric luminosity is at least  $L_{\text{tot}} \geq 6 \times 10^{33} \text{ erg s}^{-1}$ . This gives a minimum accretion rate onto the star of  $\dot{M} \sim 3 \times 10^{13} \text{ g s}^{-1}$ , and a spin-up rate ( $\dot{\nu} \sim \dot{M} (GM_* r_c)^{1/2} / (2\pi I_*)$ , where  $I_*$  is the star's moment of inertia) corresponding to

$$\dot{\nu} \sim 10^{-16} \frac{\dot{M}}{3 \times 10^{13} \text{ g s}^{-1}} \left( \frac{M_*}{1.4 M_\odot} \right)^{1/2} \left( \frac{r_c}{2.4 \times 10^6 \text{ cm}} \right)^{1/2} \left( \frac{I_*}{10^{45} \text{ g cm}^2} \right)^{-1} \text{ Hz s}^{-1} \quad (1)$$

This implies that the total accretion-related angular momentum loss is  $\sim -7 \times 10^{-16} \text{ Hz s}^{-1}$ .

J1023's low luminosity of the source (and inferred low accretion rate) suggests that it is accreting in what is usually called the 'propeller' regime ([Illarionov & Sunyaev 1975](#)). This situation can occur when the magnetic field truncates the inner disk well outside the co-rotation radius, so that the star's magnetic field spins much faster than the inner edge of the accretion flow, creating a centrifugal barrier that prevents accretion. As long as the inner edge of the disk (called  $r_m$ , the magnetospheric radius) is far from the co-rotation radius, the relative velocity between the disk and the magnetic field is large, and the magnetospheric radius can be estimated ([Arons & Lea 1976](#)):

$$r_m = \xi \left( \frac{\mu^4}{2 GM_* \dot{M}^2} \right)^{1/7} \quad (2)$$

where  $\xi \approx 0.4-1$  is a correction factor for disk accretion (see e.g. [Ghosh & Lamb 1979](#)).

However, when  $r_m$  is similar (within a factor two) to  $r_c$ , the relative rotation between the star and the inner disk is not so large, and a correct estimate for  $r_m$  must consider the relative velocity between the two ([Spruit & Taam 1993](#); [Wang 1996](#)). This estimate defines  $r_m$  as the point at which the magnetic field is strong enough to enforce gas co-rotation with the star. This yields a somewhat smaller estimate for  $r_m$  than the one

given above:

$$r_m \approx \left( \frac{\eta \mu^2}{4 \Omega_* \dot{M}} \right)^{1/5} \quad (3)$$

where  $\eta < 1$  is the relative size of the  $B_\phi$  component induced by the relative rotation between the disk and the magnetic field. Given that J1023 is accreting and being spun down, this suggests that  $r_m \sim r_c$ , thus eq. 3 is more appropriate to estimate the location of  $r_m$ .

We can use the inferred magnetospheric spin-down ( $\sim -7 \times 10^{-16} \text{ Hz s}^{-1}$ ) to set a limit on the mass outflow rate (assuming that mass ejection is responsible for spin-down). For gas outflowing at the escape velocity, the spin-down rate will be  $\dot{\nu} \sim -\dot{M}_{\text{out}} (GM_* r_m)^{1/2} / (2\pi I)$ . The outflow rate required to spin down the star by the observed amount is then

$$\dot{M} \approx 1.4 - 1.8 \times 10^{14} \text{ g s}^{-1} \left( \frac{I}{10^{45} \text{ g cm}^2} \right)^{10/9} \left( \frac{\dot{\nu}}{7 \times 10^{-16} \text{ Hz s}^{-1}} \right)^{10/9} \left( \frac{R_*}{10 \text{ km}} \right)^{-2/3} \left( \frac{B}{10^8 \text{ G}} \right)^{-2/9} \left( \frac{P_*}{1.7 \text{ ms}} \right)^{-1/9} \quad (4)$$

The range in  $\dot{M}$  comes from assuming  $\eta = 0.1 - 1$ , corresponding to a weak or strong coupling between the disk and magnetic field, and would require (on average) that only about one-fourth–one-fifth of the gas in the disk is accreted onto the star. These accretion rates correspond to an uncertainty in  $r_m \approx 1.4-2.3 r_c$ , suggesting that the centrifugal acceleration needed to launch an outflow is only likely to be strong enough if the coupling between the disk and the star is strong. (Using the conventional formula for  $r_m$  gives much weaker constraints on  $\dot{M}$  and  $r_m$ , and predicts outflows of up to  $10^{12} \text{ g s}^{-1}$ .) Numerical simulations and analytic work do not currently give strong constraints on expected outflow rates, but based on our results we conclude that the star-disk coupling may be able to drive a strong outflow, but only if the coupling is strong. If  $r_m$  stays around  $1.4 r_c$ , the coupling is unlikely to be energetic enough to launch most of the gas into an outflow, and it can remain bound, creating a trapped disk.

Whether a trapped disk forms depends on using angular momentum conservation to predict the response of the disk to interaction with the magnetic field. When the accretion rate decreases such that  $r_m > r_c$ , angular momentum conservation predicts a very different outcome from the propeller. If the rotation rate between the inner disk edge and the magnetic field is similar, the energy added by the magnetic field will not be enough to drive an efficient outflow ([Spruit & Taam 1993](#)), which can lead to an accumulation of gas in the inner regions of the disk. This will alter the gas density profile of the inner disk regions to a dead disk solution ([Sunyaev & Shakura 1977](#)). In a dead disk,  $r_m$  is no longer set by the mass accretion rate, but instead is the distance from the star where the rate angular momentum added to the disk by the disk-field interaction is balanced by the rate that viscous turbulence can transport it outward.

This solution was studied in detail by [D'Angelo & Spruit \(2010, 2011, 2012\)](#), who found that in this scenario the inner edge of the disk becomes trapped near  $r_c$  even when the accretion rate decreases by orders of magnitude (hence the term 'trapped disk'). For J1023, this implies that the observed accretion rate closely matches the actual one, and a large outflow of gas is not necessary. The angular momentum lost by the star is

then added to the accretion disk, at a rate given by

$$\dot{v} \simeq \frac{\eta \mu^2 \Delta r}{2\pi I_* r_c^3} \quad (5)$$

where  $\Delta r < 0.3$  is the width of the inner disk region that remains coupled to the magnetic field, and  $\eta$  is the strength of the coupling (introduced in eq. 3). Unfortunately, this equation has two unknown parameters:  $\eta$  and  $\Delta r$ , which could both be in the range  $\sim 0.01 - 1$  depending on the geometry of the system (e.g. the relative inclination of the magnetic field with the disk) and the poorly constrained details of the disk-field interaction. The maximum predicted net spin-down rate for J1023 is then  $\dot{v} \sim 2 \times 10^{-14}$ , while for more typical values assumed by [D’Angelo & Spruit \(2010\)](#) ( $\Delta r/r \sim 0.01 - 0.2$ ,  $\eta \sim 0.1$ ), the predicted spin down matches the observed one quite well, with  $\dot{v} \sim 10^{-16} - 10^{-15} \text{ Hz s}^{-1}$ . A drawback to the trapped disk scenario is that it does not immediately offer an explanation for why the outflow from J1023 should be more radio-bright than expected based on higher-accretion rate neutron star LMXBs. The moding behavior of J1023 may offer a clue in this regard—if unstable accretion from the trapped disk is intermittently driving a propeller (for example, in the low mode), then the additional spin-down it induces will be reduced by the moding duty cycle. However, if a trapped disk remains even in the RMSP state, any spin-down from the disk-field interaction would be folded into the overall spin-down rate, so no change would be expected. At the moment there are no observable predictions for what a trapped disk in the RMSP state would look like, but this possibility warrants further investigation.

#### 4.5. Mode Switching

A more exotic and speculative suggestion is that small amounts of accreting material could be stimulating the pulsar magnetosphere to switch between two stable luminosity modes (corresponding possibly to two stable geometric configurations of the magnetic field structure). In this model, the infalling material is not being accreted onto the surface of the neutron star and therefore this is not what is causing the observed X-ray pulsations.

Mode switching is a long-known (but poorly understood) phenomenon in rotation-powered pulsars, in which the pulse profile switches between two stable and reproducible morphologies (e.g., [Bilous et al. 2014](#)). It is sometimes accompanied by noticeable changes in the spin-down rate ([Kramer et al. 2006](#); [Lyne et al. 2010](#)), though not always. In some moding pulsars only upper limits on the spin-down change are available (cf. [Young et al. 2012](#)).

Recent observations of PSR B0943+10 showed that the radio pulse profile changes can be accompanied by simultaneous switches in the X-ray pulse profile and brightness ([Hermesen et al. 2013](#)). Similarly, the radio-quiet  $\gamma$ -ray pulsar PSR J2021+4026, in the Gamma Cygni region, has also shown a sudden profile change accompanied by a spin-down rate change ([Allafort et al. 2013](#)). Moding has never been seen in an RMSP or AMXP, nor is it believed to be associated with accretion. Nonetheless, the idea that moding, nulling, and intermittency may be associated with changes in the plasma density of the pulsar magnetosphere lead us to speculate that this effect could also be induced by small amounts of accretion matter entering the magnetosphere. That said, in this scenario, it is completely unclear how material parked at the light cylinder can move in and out about this radius to trigger the mode

switching. Nonetheless, the rapid switches in J1023’s X-ray light curve between low and high modes is reminiscent of the abrupt switches seen in pulsar moding, and we also know that the X-ray pulsations are also switching on/off at these times. However, this is only a qualitative similarity. Though it is likely impossible from a practical point-of-view (there are of order  $10$  *Fermi*-detected  $\gamma$ -ray photons from J1023 during all the *XMM-Newton* X-ray observations presented here), if one could show that the  $\gamma$ -rays are generated only in the low or high mode, then one could plausibly argue that the X-ray pulsations are due to heating of the magnetic polar caps, not by the accretion flow itself but by the normal rotation-powered mechanism also responsible for the observed X-ray pulsations in the RMSP state.

## 5. CONCLUSIONS & FUTURE WORK

By phase connecting a set of nine *XMM-Newton* observations, we have shown that J1023 spins down on average 26.8% faster since 2013 June, when it transitioned from a rotation-powered RMSP state to an accretion-powered LMXB state. This is the first time that it has been possible to make such a comparison for a tMSP system, and it shows that the accretion torques during the LMXB state are modest compared to the primary spin-down driver that is also present in the RMSP state (i.e. the pulsar wind). The rich observational phenomena displayed by J1023 has also been seen in the other confirmed tMSPs, namely XSS J12270–4859 and IGR J18245–2452. As such, there is good reason to expect this behavior to be typical of tMSPs in the ‘intermediate’ accretion LMXB state ([Linares 2014](#)).

J1023 can continue to be timed in the LMXB state, in order to confirm that the average spin-down rate observed up until now will persist. Unfortunately, the only instrument capable of providing the necessary observations is *XMM-Newton* in the EPIC-pn timing mode. Such observations are only possible in two  $\sim 1.5$  month windows per year, when J1023 (a nearly ecliptic source) is not in the Sun constraint. Continued timing is most strongly motivated by the desire to provide a continued baseline that can be connected to the timing measurements that will undoubtedly follow once the source reignites as an observable RMSP. If continued timing across a future LMXB to RMSP state transition shows a sudden jump in the spin frequency and its derivative, it can potentially help us understand the torques acting on the neutron star during such a transition. Lastly, though the stochastic orbital variations of J1023 will make it challenging, an unbroken timing solution is necessary for attempts to detect pulsed  $\gamma$ -rays from the ongoing *Fermi* observations.

## 6. ACKNOWLEDGEMENTS

The authors gratefully thank Lucien Kuiper for his insights into the EPIC-pn timing mode as well as Ben Stappers and Andrew Lyne for their previous contributions to timing J1023 in the RMSP state. A.J., J.W.T.H. and C.B. acknowledge funding from the European Research Council under the European Union’s Seventh Framework Programme (FP7/2007-2013) / ERC grant agreement no. 337062 (DRAGNET). A.M.A acknowledges support from an NWO Veni Fellowship. A.P. and C.D’A. acknowledge support from an NWO Vidi Fellowship. This work was funded in part by NASA grant NNX15AJ50G awarded through Columbia University. The results presented in this paper were based on observations obtained with *XMM-Newton*, an ESA science mission with instruments and contributions directly funded by ESA Member States and NASA.

We thank Norbert Scharrel and the *XMM-Newton* observatory for granting these DDT observations on short notice. The Arecibo Observatory is operated by SRI International under a cooperative agreement with the NSF (AST-1100968), and in alliance with Ana G. Méndez-Universidad Metropolitana, and the Universities Space Research Association. We have made extensive use of the NASA Astrophysics Data System (ADS) and the arXiv. A.J. and J.W.T.H would like to extend thanks to Joel Weisberg for helpful discussions. A.J. would also like to thank F. Coti Zelati for comments on an initial draft. Lastly, we acknowledge the International Space Science Institute (ISSI) that funded an international team devoted to the study of transitional millisecond pulsars where this work has been discussed, and we thank all the members of the team for fruitful discussions.

## REFERENCES

- Allafort, A., Baldini, L., Ballet, J., et al. 2013, *ApJL*, 777, L2
- Alpar, M. A., Cheng, A. F., Ruderman, M. A., & Shaham, J. 1982, *Nature*, 300, 728
- Aly, J. J., & Kuijpers, J. 1990, *A&A*, 227, 473
- Archibald, A. M., Kaspi, V. M., Bogdanov, S., et al. 2010, *ApJ*, 722, 88
- Archibald, A. M., Kaspi, V. M., Hessels, J. W. T., et al. 2013, *ArXiv e-prints*, arXiv:1311.5161
- Archibald, A. M., Stairs, I. H., Ransom, S. M., et al. 2009, *Science*, 324, 1411
- Archibald, A. M., Bogdanov, S., Patruno, A., et al. 2015, *ApJ*, 807, 62
- Arons, J., & Lea, S. M. 1976, *ApJ*, 207, 914
- Bassa, C. G., Patruno, A., Hessels, J. W. T., et al. 2014, *MNRAS*, 441, 1825
- Bednarek, W. 2015, *MNRAS*, 451, L55
- Bednarek, W., & Banasiński, P. 2015, *Journal of High Energy Astrophysics*, 8, 21
- Bilous, A. V., Hessels, J. W. T., Kondratiev, V. I., et al. 2014, *A&A*, 572, A52
- Bogdanov, S., Archibald, A. M., Hessels, J. W. T., et al. 2011, *ApJ*, 742, 97
- Bogdanov, S., & Halpern, J. P. 2015, *ApJL*, 803, L27
- Bogdanov, S., Archibald, A. M., Bassa, C., et al. 2015, *ApJ*, 806, 148
- Breton, R. P., van Kerkwijk, M. H., Roberts, M. S. E., et al. 2013, *ApJ*, 769, 108
- Burderi, L., Di Salvo, T., D'Antona, F., Robba, N. R., & Testa, V. 2003, *A&A*, 404, L43
- Burderi, L., Possenti, A., D'Antona, F., et al. 2001, *ApJL*, 560, L71
- Chakrabarty, D., Morgan, E. H., Munro, M. P., et al. 2003, *Nature*, 424, 42
- Coti Zelati, F., Baglio, M. C., Campana, S., et al. 2014, *MNRAS*, 444, 1783
- Cuevas, A., & Romo, J. 1993, *Journal of Statistical Planning and Inference*, 37, 181
- D'Angelo, C. R., Fridriksson, J. K., Messenger, C., & Patruno, A. 2015, *MNRAS*, 449, 2803
- D'Angelo, C. R., & Spruit, H. C. 2010, *MNRAS*, 406, 1208
- , 2011, *MNRAS*, 416, 893
- , 2012, *MNRAS*, 420, 416
- de Jager, O. C., Raubenheimer, B. C., & Swanepoel, J. W. H. 1989, *A&A*, 221, 180
- Deller, A. T., Archibald, A. M., Briskin, W. F., et al. 2012, *ApJL*, 756, L25
- Deller, A. T., Moldon, J., Miller-Jones, J. C. A., et al. 2015, *ApJ*, 809, 13
- di Salvo, T., Burderi, L., Riggio, A., Papitto, A., & Menna, M. T. 2008, *MNRAS*, 389, 1851
- Edwards, R. T., Hobbs, G., & Manchester, R. 2006, *Mon.Not.Roy.Astron.Soc.*, 372, 1549
- Ghosh, P., & Lamb, F. K. 1979, *ApJ*, 232, 259
- Goldreich, P., & Julian, W. H. 1969, *ApJ*, 157, 869
- Goodson, A. P., Winglee, R. M., & Boehm, K. 1997, *ApJ*, 489, 199
- Hartman, J. M., Galloway, D. K., & Chakrabarty, D. 2011, *ApJ*, 726, 26
- Hartman, J. M., Patruno, A., Chakrabarty, D., et al. 2008, *ApJ*, 675, 1468
- Hayashi, M. R., Shibata, K., & Matsumoto, R. 1996, *ApJL*, 468, L37+
- Hermesen, W., Hessels, J. W. T., Kuiper, L., et al. 2013, *Science*, 339, 436
- Hessels, J. W. T., Ransom, S. M., Stairs, I. H., et al. 2006, *Science*, 311, 1901
- Hobbs, G., Edwards, R., & Manchester, R. 2006, *Mon.Not.Roy.Astron.Soc.*, 369, 655
- Illarionov, A. F., & Sunyaev, R. A. 1975, *A&A*, 39, 185
- Kramer, M., Lyne, A. G., O'Brien, J. T., Jordan, C. A., & Lorimer, D. R. 2006, *Science*, 312, 549
- Li, J., Spitkovsky, A., & Tchekhovskoy, A. 2012, *ApJL*, 746, L24
- Lii, P. S., Romanova, M. M., Ustyugova, G. V., Koldoba, A. V., & Lovelace, R. V. E. 2014, *MNRAS*, 441, 86
- Linares, M. 2014, *ApJ*, 795, 72
- Lovelace, R. V. E., Romanova, M. M., & Bisnovatyi-Kogan, G. S. 1995, *MNRAS*, 275, 244
- Lyne, A., Hobbs, G., Kramer, M., Stairs, I., & Stappers, B. 2010, *Science*, 329, 408
- Martin-Carrillo, A., Kirsch, M. G. F., Caballero, I., et al. 2012, *A&A*, 545, A126
- Mason, K. O., Breeveld, A., Much, R., et al. 2001, *A&A*, 365, L36
- Miller, K. A., & Stone, J. M. 1997, *ApJ*, 489, 890
- Papitto, A., de Martino, D., Belloni, T. M., et al. 2015, *MNRAS*, 449, L26
- Papitto, A., Riggio, A., Burderi, L., et al. 2011, *A&A*, 528, A55
- Papitto, A., & Torres, D. F. 2015, *ApJ*, 807, 33
- Papitto, A., Ferrigno, C., Bozzo, E., et al. 2013a, *Nature*, 501, 517
- Papitto, A., Hessels, J. W. T., Burgay, M., et al. 2013b, *The Astronomer's Telegram*, 5069, 1
- Parfrey, K., Spitkovsky, A., & Beloborodov, A. M. 2015, *ArXiv e-prints*, arXiv:1507.08627
- Patruno, A. 2010, *ApJ*, 722, 909
- Patruno, A., Bult, P., Gopakumar, A., et al. 2012, *ApJL*, 746, L27
- Patruno, A., & Watts, A. L. 2012, *ArXiv e-prints*, arXiv:1206.2727
- Patruno, A., Wijnands, R., & van der Klis, M. 2009, *ApJL*, 698, L60
- Patruno, A., Archibald, A. M., Hessels, J. W. T., et al. 2014, *ApJL*, 781, L3
- Radhakrishnan, V., & Srinivasan, G. 1982, *Current Science*, 51, 1096
- Ransom, S. M., Stairs, I. H., Archibald, A. M., et al. 2014, *Nature*, 505, 520
- Rees, M. J., Begelman, M. C., Blandford, R. D., & Phinney, E. S. 1982, *Nature*, 295, 17
- Riggio, A., Burderi, L., di Salvo, T., et al. 2011, *A&A*, 531, A140
- Roberts, M. S. E. 2013, in *IAU Symposium*, Vol. 291, *IAU Symposium*, ed. J. van Leeuwen, 127–132
- Romanova, M. M., Ustyugova, G. V., Koldoba, A. V., & Lovelace, R. V. E. 2004, *ApJL*, 616, L151
- Shvartsman, V. F. 1971, *AZh*, 48, 438
- Spitkovsky, A. 2006, *ApJL*, 648, L51
- Spruit, H. C., & Taam, R. E. 1993, *ApJ*, 402, 593
- Stappers, B. W., Archibald, A., Bassa, C., et al. 2013, *The Astronomer's Telegram*, 5513, 1
- Stappers, B. W., Archibald, A. M., Hessels, J. W. T., et al. 2014, *ApJ*, 790, 39
- Strüder, L., Briel, U., Dennerl, K., et al. 2001, *A&A*, 365, L18
- Sunyaev, R. A., & Shakura, N. I. 1975, *Soviet Astronomy Letters*, 1, 158
- , 1977, *Soviet Astronomy Letters*, 3, 138
- Takata, J., Li, K. L., Leung, G. C. K., et al. 2014, *The Astrophysical Journal*, 785, L31
- Takata, J., Li, K. L., Leung, G. C. K., et al. 2014, *ApJ*, 785, 131
- Tam, P. H. T., Li, K. L., Kong, A. K. H., et al. 2014, *ArXiv e-prints*, arXiv:1412.4985
- Taylor, J. H., & Weisberg, J. M. 1989, *ApJ*, 345, 434
- Tendulkar, S. P., Yang, C., An, H., et al. 2014, in *AAS/High Energy Astrophysics Division*, Vol. 14, *AAS/High Energy Astrophysics Division*, 122–23
- Thorstensen, J. R., & Armstrong, E. 2005, *AJ*, 130, 759
- Turner, M. J. L., Abbey, A., Arnaud, M., et al. 2001, *A&A*, 365, L27
- Uzdensky, D. A. 2004, *Ap&SS*, 292, 573
- Uzdensky, D. A., Königl, A., & Litwin, C. 2002, *ApJ*, 565, 1191
- van Straten, W., & Bailes, M. 2011, *PASA*, 28, 1
- Wackernagel, H. 2003, *Multivariate Geostatistics* (Springer, Germany)
- Wang, Y.-M. 1996, *ApJL*, 465, L111
- Watts, A. L. 2012, *Annual Review of Astronomy and Astrophysics*, 50, 609
- Wijnands, R., & van der Klis, M. 1998, *Nature*, 394, 344
- Young, N. J., Stappers, B. W., Weltevrede, P., Lyne, A. G., & Kramer, M. 2012, *MNRAS*, 427, 114
- Zanni, C., & Ferreira, J. 2013, *A&A*, 550, A99

## APPENDIX

### SEPARATION OF ORBITAL AND SPIN-DOWN EFFECTS

Traditionally, in pulsar timing, a model is constructed to predict pulse arrival phase, including astrometric, rotational, and orbital effects. This works well for some pulsars, but for pulsars with more complex behavior—e.g. stochastic “red” variations of the pulsar spin-down or stochastic variations of orbital parameters—attempting to parametrize that complex behavior can become complex and awkward. It can also become difficult to distinguish variations in orbital parameters from variations in intrinsic pulsar spin-down. We therefore describe an approach that allows clean separation of orbital effects from intrinsic pulsar spin-down. This proceeds essentially by removing the propagation delay across the orbit (where the orbital model may vary from epoch to epoch), yielding

pulse emission times as measured at the pulsar position; these emission times can then be treated as if the pulsar were isolated.

Pulsar orbital models vary in complexity. Some pulsars are adequately modeled with Keplerian orbital models, but many require more complex models. Many pulsar systems are sufficiently relativistic to require “parameterized post-Keplerian” models in which the Keplerian orbital elements change with time. One millisecond pulsar is known in a stellar triple system (Ransom et al. 2014), where even Newtonian interactions between the two orbits produce substantial deviations from Keplerian models. Other systems, particularly the black widow and redback interacting-binary systems, undergo stochastic orbital variations due to poorly understood processes (possibly quadrupole-moment changes within the companion; for a discussion see Archibald et al. 2013), requiring orbital models flexible enough to accommodate substantial deviations from a Keplerian model (traditionally parameterized by allowing multiple derivatives of orbital parameters).

Given a model for the orbit of a pulsar, observed pulse arrival times are converted to a time scale called pulsar emission time. This conversion involves the removal of delays due to propagation across the pulsar system (both geometric and relativistic Shapiro delay), propagation across the solar system (again, both geometric and Shapiro delays), interstellar propagation (dispersion), and relativistic time dilation at both the Earth and the pulsar. It should be noted that the pulsar emission time scale is conventionally rescaled so that its mean rate equals that of the Earth’s, so only the varying component of the time dilation appears in the conversion. Once arrival times have been converted to this pulsar emission time scale, the pulsar spin-down model allows conversion of emission time to phase. This typically uses simple linear model parameterized by spin frequency at some specified epoch and spin frequency derivative. Pulsars with more complex spin-frequency behavior may require more complex models: stable young pulsars may have a measurable second frequency derivative (permitting the calculation of a braking index); glitching pulsars may require a model with phase, frequency, and/or frequency-derivative jumps; pulsars with spin-down noise require a more complex model, often represented as a polynomial parameterized by multiple higher-order frequency derivatives.

The pulsar emission time provides a place to separate the problem of describing the pulsar orbit from that of describing the pulsar’s intrinsic spin-down. Specifically, we wish to work with a system in which the orbital parameters vary stochastically. We seek to study the intrinsic spin-down of the pulsar. In this paper, our observations are *XMM-Newton* X-ray observations each spanning more than a complete binary orbit. For each epoch, then, we fit for the varying orbital parameters to obtain an orbital model specific to that epoch, using the pulse profile signal-to-noise ( $H$  score) as a measure of goodness-of-fit. Thus, in principle, we should be able to use these orbital models to obtain pulsar emission times for each observed pulse.

Existing pulsar-timing tools (e.g. `tempo` and `tempo2`) are not designed to work with pulsar emission times, though they necessarily compute them internally. We are therefore forced to use a more complex analysis procedure. We begin with an ephemeris based on the timing of the system in the RMSP state. This allows us to compute phases for each photon from an X-ray observation; since previous work showed that adjusting the time of the ascending node ( $T_{\text{asc}}$ ) was sufficient to model the orbital variations, we adjust  $T_{\text{asc}}$  for each observation to maximize the  $H$  score of the pulsations. We use this  $T_{\text{asc}}$  adjusted ephemeris to compute photon phases and obtain a folded pulse profile. We then cross-correlate this folded profile against a template (obtained from the observation with the best signal-to-noise) and obtain a phase shift of the observed pulse relative to the pulse predicted by the ephemeris. This requires some care: since `tempo` is not ordinarily concerned with absolute pulse phases, it always sets the phase of the first event to zero. We therefore introduce a synthetic event, the same for each observation, to define the zero of phase (we choose MJD 56480, the nominal date of radio disappearance).

Here, a subtlety arises: the zero of phase should be defined in the pulsar emission time scale in order to be truly consistent between observations with different orbital parameters, but neither `tempo` nor `tempo2` allow the specification of times in this time scale. We therefore perform an inversion process so that our synthetic event occurs at MJD 56480 in the pulsar emission time scale. A second concern is that uncertainties in orbital parameter determination affect the computed pulsar emission times and therefore the computed phases; we therefore include the process of fitting for  $T_{\text{asc}}$  in our bootstrap-based estimation of the uncertainties on the pulse phase. Through this process we obtain a set of phase residuals relative to the given spin ephemeris, which allows us to compute needed changes in spin frequency or frequency derivative as if the pulsar were isolated. We confirm that these changes produce the intended effect by reprocessing the photons with the modified ephemeris; indeed, the residuals shift by the claimed amount and yield a reasonable fit.

As a cross-check of this method, we note that the orbital evolution post-disappearance can be modeled by a single `tempo` parameter file that includes appropriate  $T_{\text{asc}}$ ,  $P_{\text{orb}}$  and  $\dot{P}_{\text{orb}}$ . These values can be found by fitting the  $T_{\text{asc}}$  values from individual observations, and this ephemeris yields residual  $\Delta T_{\text{asc}}$  values on the order of a second. Folding all the photons with this single ephemeris results in some amount of profile smearing, but the pulsations remain detectable, and phases (pulse arrival times) can be extracted from these profiles. We are therefore able to directly compare the pulse phases computed using a traditional `tempo` parameter file to those obtained using our new method; the last panel of Fig. 5 shows that the phases are very similar, validating this new technique.

We believe that working with the pulsar emission time scale is helpful in dealing with pulsars with complex spin down behavior. We suggest a relatively minor change to `tempo` and `tempo2` to make this easier: in addition to the “observatory codes” ‘@’ and ‘0’, which indicate that times are measured at the solar system and Earth barycenters, respectively, we suggest an additional “observatory code,” e.g. ‘\*’, to indicate that a time is measured in pulsar emission time. We note that `tempo2`’s ‘general2’ output plugin already permits the output of pulsar emission time for any event (although we caution readers that older versions contained a sign error in its calculation). The addition of the observatory code ‘\*’ `tempo/tempo2` would greatly ease working with timing data from redbacks, black widows, and binary pulsars with complex spin-down behavior.

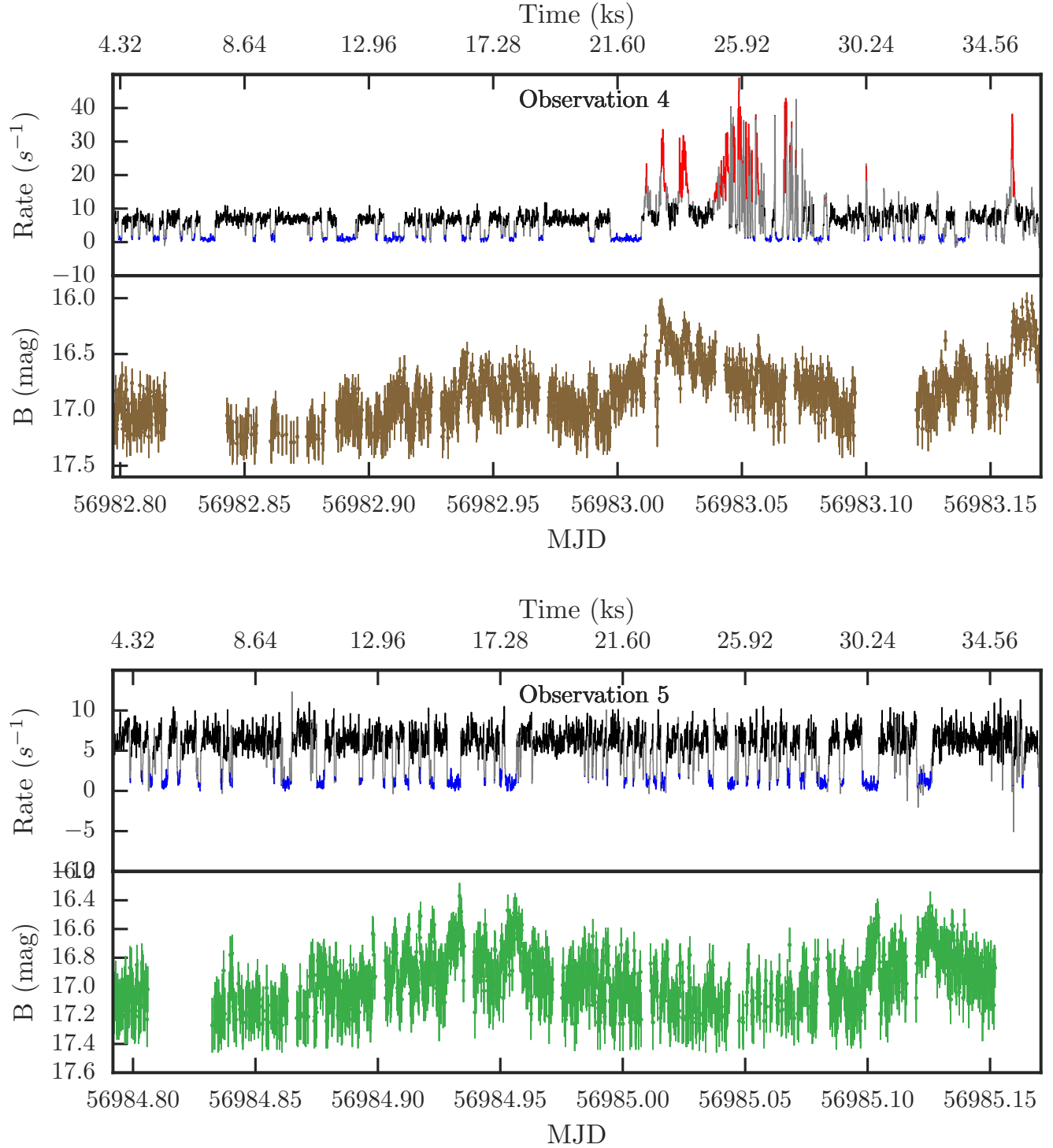


**Figure 7.** X-ray and optical lightcurves of PSR J1023+0038 for Obs. 4 and 5 (see Table 1). The top panels of each observation show the X-ray light curve obtained by adding pn, MOS1, and MOS2 data from *XMM-Newton* (each background subtracted and exposure corrected). Black, blue and red colours are used to depict high, low and flare mode, respectively. The bottom panel in each observation represents the *XMM-Newton* B-filter optical lightcurve. Note that, since the *XMM-Newton* OM observations start earlier than *XMM-Newton* EPIC-pn, the start times in above plots are limited by Epic-pn.

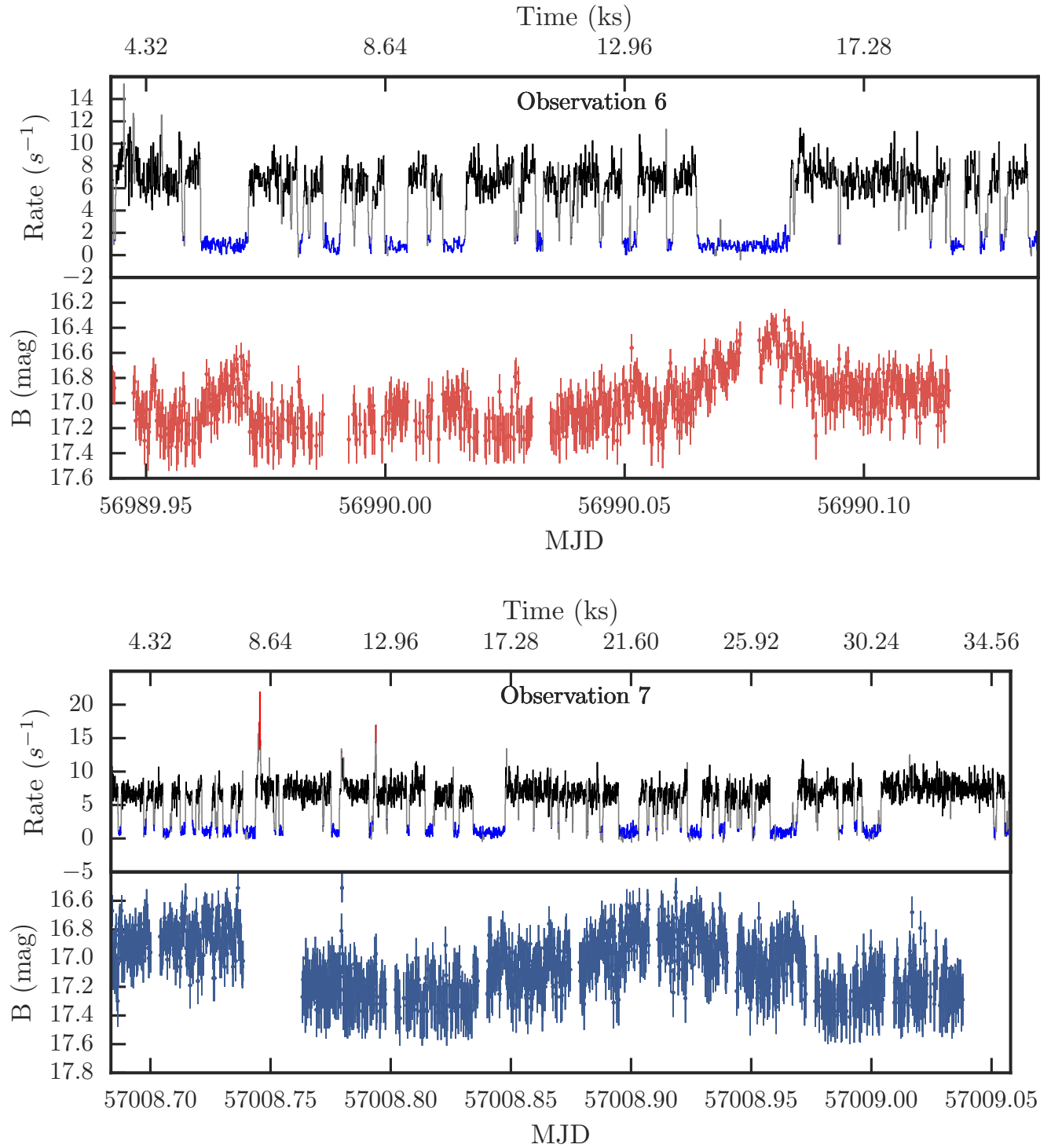


**Figure 7 (Cont.).** X-ray and optical lightcurves of PSR J1023+0038 for Obs. 6 and 7 (see Table 1). The top panels of each observation show the X-ray light curve obtained by adding pn, MOS1, and MOS2 data from *XMM-Newton* (each background subtracted and exposure corrected). Black, blue and red colours are used to depict high, low and flare mode, respectively. The bottom panel in each observation represents the *XMM-Newton* *B*-filter optical lightcurve. Note that, since the *XMM-Newton* OM observations start earlier than *XMM-Newton* EPIC-pn, the start times in above plots are limited by Epic-pn.

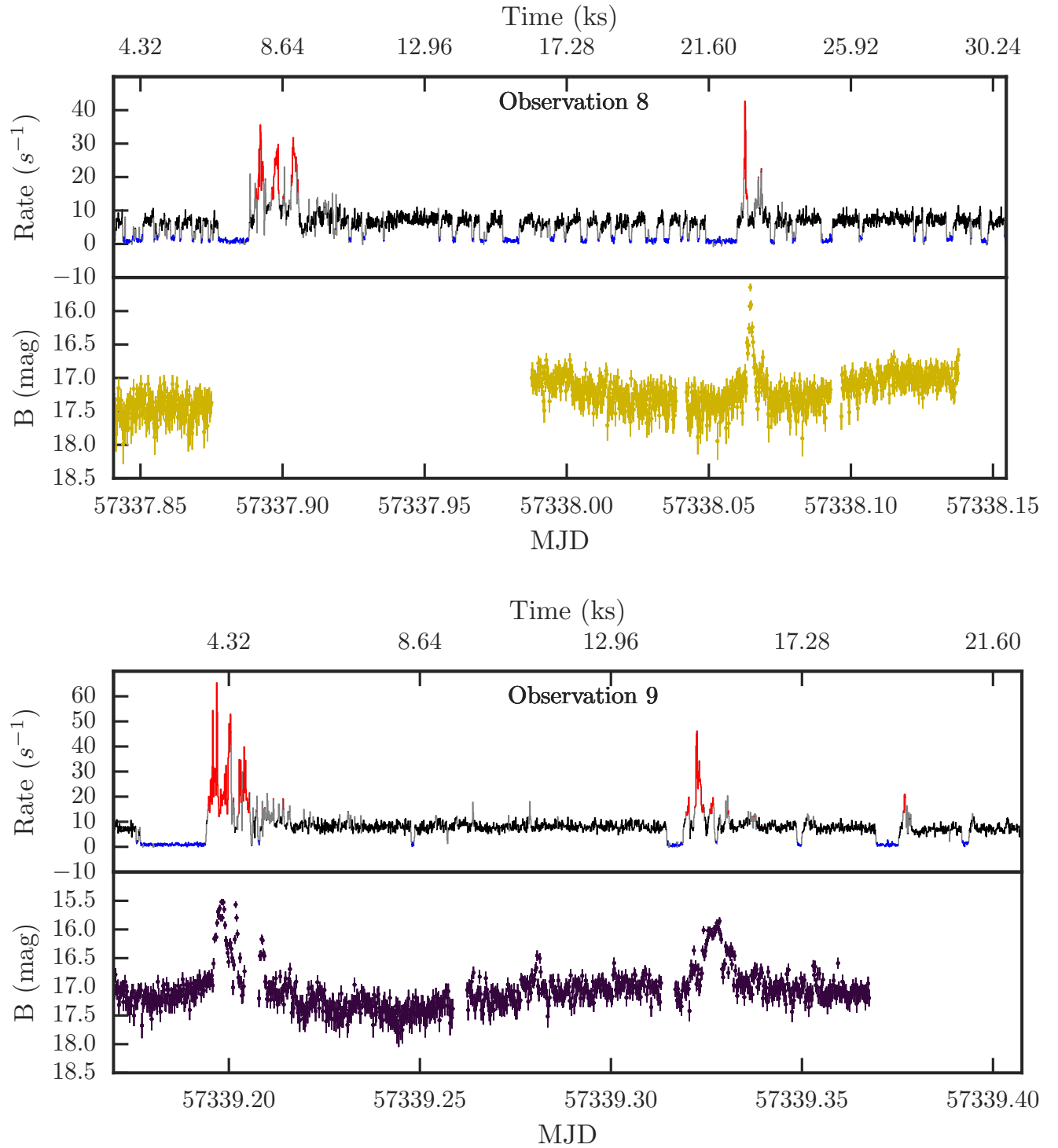


**Figure 7 (Cont.).** X-ray and optical lightcurves of PSR J1023+0038 for Obs. 8 and 9 (see Table 1). The top panels of each observation show the X-ray light curve obtained by adding pn, MOS1, and MOS2 data from *XMM-Newton* (each background subtracted and exposure corrected). Black, blue and red colours are used to depict high, low and flare mode, respectively. The bottom panel in each observation represents the *XMM-Newton*  $B$ -filter optical lightcurve. Note that, since the *XMM-Newton* OM observations start earlier than *XMM-Newton* EPIC-pn, the start times in above plots are limited by Epic-pn.

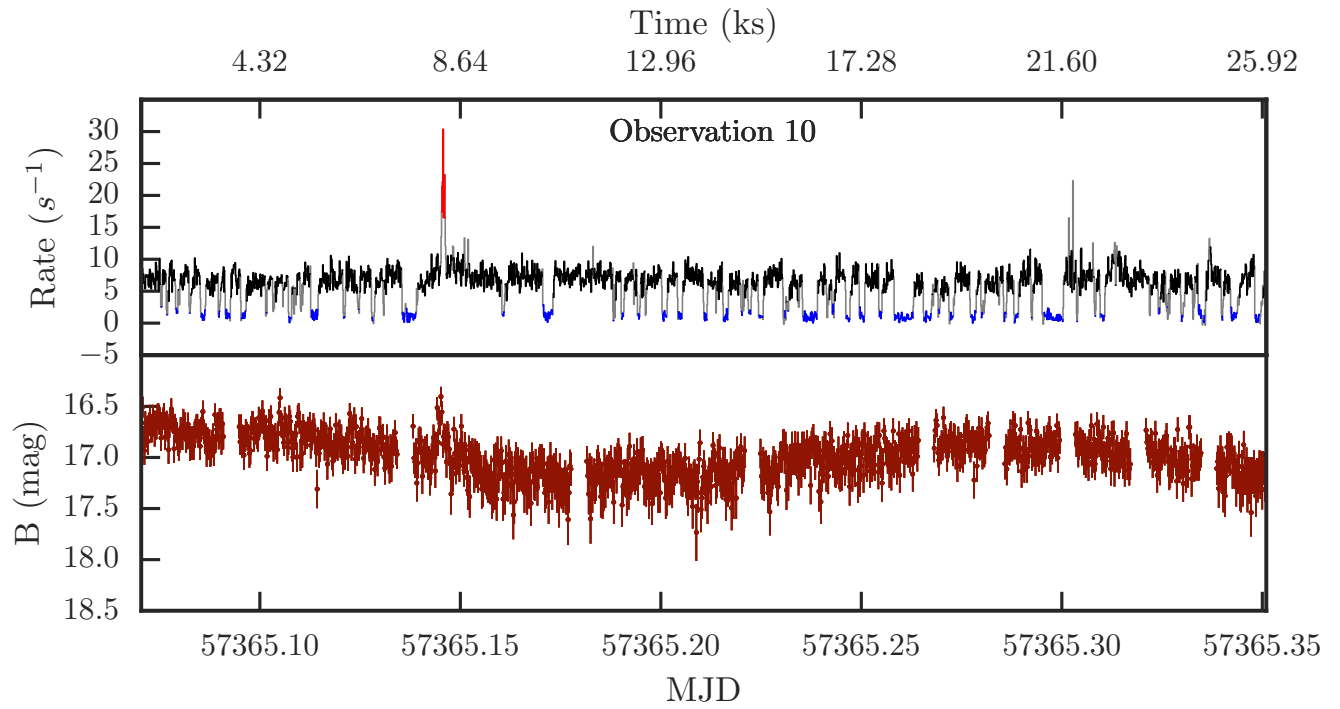


**Figure 7 (Cont.).** X-ray and optical lightcurves of PSR J1023+0038 for Obs. 10 (see Table 1). The top panel shows the X-ray light curve obtained by adding pn, MOS1, and MOS2 data from *XMM-Newton* (each background subtracted and exposure corrected). Black, blue and red colours are used to depict high, low and flare mode, respectively. The bottom panel in each observation represents the *XMM-Newton* B-filter optical lightcurve. Note that, since the *XMM-Newton* OM observations start earlier than *XMM-Newton* EPIC-pn, the start times in above plots are limited by Epic-pn.